

CHAPTER 1

HIGH DENSITY MAGNETIC DATA STORAGE

Huimeng Wu

Chemistry Department, University of Florida, Gainesville, FL 32611, USA
E-mail: huimeng@ufl.edu

Li Zhang

Department of Applied Physics, University of Electronic Science and Technology of China, Chengdu 610054, P. R. China
E-mail: zhangli_cmu2005@yahoo.com.cn

Yanlin Song

Beijing National Laboratory for Molecular Sciences
Key Laboratory of Organic Solids, Institute of Chemistry
Chinese Academy of Sciences, Beijing 100190, China
E-mail: ylsong@iccas.ac.cn

Areal density in magnetic data storage can be increased by the scaling method. However, the increase cannot continue indefinitely, due to the limit of fabrication technology and thermal stability. To postpone the onset of thermal instability, materials with high magnetic anisotropy are required for recording media in conventional longitudinal magnetic data storage. Nevertheless, this method is limited in further increasing the recording density because it requires extremely huge write field for high anisotropy media. Therefore, to achieve ultrahigh density magnetic data storage, alternative methods has to be explored. This chapter highlights recent advanced technologies and research work proposed for ultrahigh density magnetic data storage, including perpendicular recording, patterned media storage, self-assembling media and molecule-based magnets.

1. Introduction

In order to meet the rapid growing capacity of data storage, ever-increasing areal densities and data rates are needed. Magnetic recording, as one of the most important technologies in data storage, has received enormous

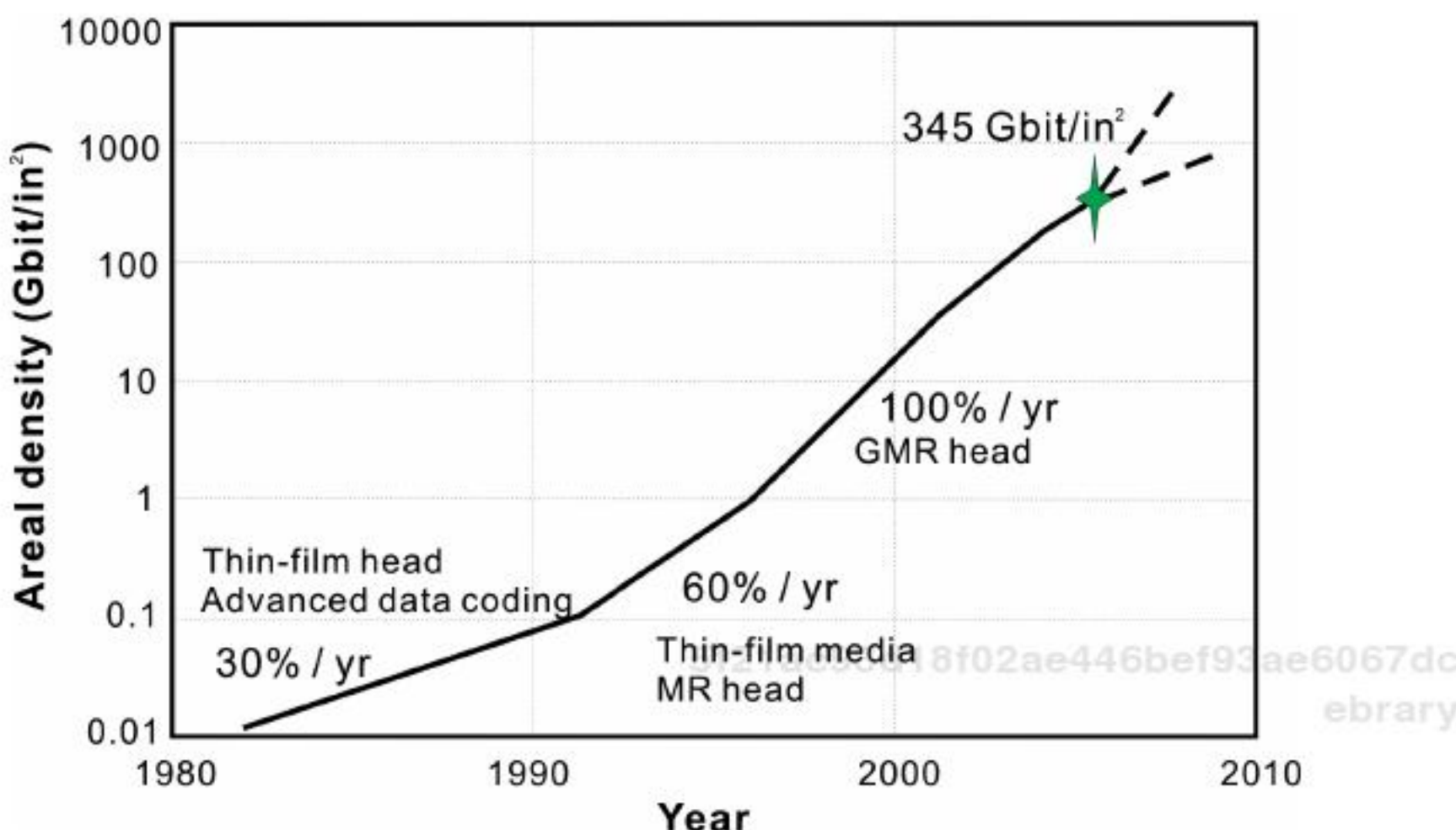


Fig. 1. Areal density for magnetic data recording. (Adapted from Ref. 1 with permission, © 1999, Academic Press).

attention. Figure 1 shows the trend in areal density of magnetic data storage during the past 30 years. Before 1990, the data storage capacity increased at about 30% per year, which arose from the introduction of the thin-film head and advanced data coding. Then a 60% growth rate began in 1991, which was caused by the applications of the magnetoresistive head (MR) and thin-film recording media.¹ During the late 1990s, the areal density of the hard disk increased by over 100% per annum through the introduction of a giant magnetoresistive (GMR) reading sensor.

Since then, higher areal density has been achieved by scaling the components of the disk drive and/or using high K_u (magnetic anisotropy) alternative recording media. Scaling methods can decrease the dimension of recording media, the geometry of the read–write head and the head–media spacing. However, scaling cannot continue indefinitely because of the limit of fabrication technology and thermal stability. Higher K_u materials maintain thermal stability at smaller grain size, but require stronger magnetic field to switch the magnetization of bits, which could be beyond the capability of the write head. In fact, we are already approaching the limitation of thermal stability for the conventional longitudinal recording method.^{3,4} In order to further increase the areal density of magnetic data storage, alternative method must be explored for ultrahigh density data

storage. In September 2006, an areal density of 345 Gbits/in² in perpendicular recording was demonstrated in laboratory by Hitachi Global Storage Technologies.² Nonetheless, this still cannot fulfill the rapidly increasing requirement of information capacity. The pursuit of ultrahigh density data storage still continues. Furthermore, other approaches are proposed besides perpendicular recording.

This chapter will begin with the basic theory of magnetic recording. This will be followed by the current magnetic recording technologies and the limitation set by the thermal instability. Then, some of the recently implemented and promising technologies and research work for ultrahigh density data storage will be reviewed. This chapter focuses primarily on the recording media and some recording mechanisms will also be discussed.

2. Theory of Magnetic Recording

2.1. *Magnetic states of matter*

Magnetic moment of electrons originates from two kinds of electron moments. One, associated with an intrinsic angular momentum of the electron, is called the intrinsic spin magnetic dipole moment. The other, associated with the electron orbit surrounding the nucleus, is called orbital magnetic dipole moment. The total moment of the electron is the combination of those two. Typically, spin magnetic dipole moment is much greater than the orbital one. Consequently, the orbital magnetic dipole moment may be neglected. The magnetic moment of an atom is the total magnetic moments of all the electrons inside the atom. Finally, all the atoms' magnetic moments in a substance combine collectively to produce the magnetic moment of the substance. Therefore, the differences in electron configurations determine the different magnetic properties of a substance. Based on various electronic configurations, magnetic materials can be categorized into several types: diamagnets (e.g. copper and gold), paramagnets (e.g. aluminum and manganese), ferromagnets (e.g. iron, cobalt, nickel, gadolinium, dysprosium and permalloy), ferrimagnets (e.g. Fe₃O₄) and antiferromagnets (e.g. MnO).

Diamagnetic materials have paired electrons and compensated electron moments. When an external magnetic field is applied, their magnetic

moments prefer to align opposite to the field and create a weak, negative magnetic susceptibility. Magnetic susceptibility χ is defined by $\chi = M/H$, where M is magnetization of the material, a measure of the magnetic moment per unit volume; and H is the external magnetic field. The value of χ is the extent to which a material may be magnetized in response to a given applied magnetic field. Typically, diamagnetic molar susceptibilities are very small and independent of the strength of the external magnetic field and temperature.

Unlike diamagnets, other magnets contain unpaired electrons. The alignment of the unpaired electrons spinning through the exchange interaction in each magnetic domain generates a spontaneous magnetization. The interaction between the two unpaired electrons can be described by the following equation:

$$E_{\text{ex}} = -2J_{ij}\vec{s}_i \cdot \vec{s}_j$$

where \vec{s}_i and \vec{s}_j are electron spin vectors of atoms i and j respectively, and J_{ij} is the exchange integral determined by an integration over the overlapping wave functions of those two electrons. If $J_{ij} = 0$, there is no interaction and the substance exhibits the paramagnetic property. If $J_{ij} > 0$, the spins tend to be parallel, leading to ferromagnetism. If $J_{ij} < 0$, the spins are in antiparallel, leading to anti-ferromagnetism.

For paramagnets, each dipole on each atom or ion does not interact with other one in the absence of an external field. When placed in a field, those random oriented dipoles will align and result in a net magnetization. However, when the field is removed, the alignment will be quickly disrupted by thermal perturbation, resulting in a zero net magnetization. Paramagnetic susceptibility is temperature-dependent. When the temperature increases, the magnetic susceptibility χ will decrease because the thermal agitation makes aligning the individual magnetic moments difficult. When the temperature is fixed and the applied field is increased, the magnetization will increase because the external field can suppress thermal agitation and align magnetic moments. Generally, magnetic susceptibility of paramagnets is weak.

For ferromagnets, individual atomic spin moments interact with each other and align spontaneously in the absence of an external field. In each

magnetic domain, the spin moments align in the same direction and create a net magnetization. But the alignment of spin moments varies in different domains, resulting in an unmagnetized bulk sample in most cases. When an external field is applied, the magnetic domains line up with each other and a magnetic field will be generated inside the material. The internal magnetic field can be even stronger than the external applied one. This signifies that these materials have a large positive magnetic susceptibility. Unlike paramagnets, when the applied field is removed, ferromagnets will still keep a portion of magnetization in the direction of the external field. However, when the temperature increases to a certain point (called the Curie temperature, T_C), the thermal energy exceeds the spin coupling (exchange) energy, and the arrangement of magnetic domains breaks down. Thus, at high temperature, ferromagnets will lose their ferromagnetism and behave like a paramagnet.

Since the exchange coupling of individual atomic spin moments in each magnetic domain does not always lead to parallel alignment of all spins, antiferromagnets and ferrimagnets should also be considered.

In antiferromagnets, each atomic spin moment is opposite to adjacent ones spontaneously. As a result the net magnetic moment of the material is zero. But due to spin canting, lattice defects and frustrated surface spins in nanoscale particles, antiferromagnetic materials may exhibit a weak net magnetization. The spontaneous antiparallel coupling of atomic magnets can be disrupted by heating. At a very low temperature, an antiferromagnetic material exhibits no response to the external field, because the antiparallel ordering of atomic spin moments is rigidly retained. But at higher temperature, some atomic magnetic moments break free from the orderly arrangement and align with the external field. When temperature further increases to the transition temperature (called the Néel temperature, T_N), the material reaches a maximum magnetization. Beyond this temperature, thermal energy progressively prevents alignment with the magnetic field. Then the magnetism caused by the alignment of atomic magnetic moments continuously decreases as temperature is increased. The typical Néel temperatures are low, e.g. T_N of MnO is 122 K. While some antiferromagnetic materials can have very high Néel temperatures, even several hundred °C above the room temperature.

The exchange interactions in ferrimagnets lead to parallel alignment of atomic spin moments in some crystal sites and antiparallel alignment in others. Unlike antiferromagnets, the opposing moments in ferrimagnets are not equal and generate a net magnetization. Compared with a ferromagnetic material, a ferrimagnetic material has a very similar magnetic behavior, but a different magnetic ordering. Actually, ferrimagnetism is observed only in some compounds that have complex crystal structures. One important example is magnetite (Fe_3O_4), in which two trivalent iron ions align with opposite moments and cancel each other, and so the net moment arises from the divalent iron ion.

5f21ac93d18f02ae446bef93ae6067dc
ebrary

2.2. Magnetic hysteresis

As mentioned before, a ferromagnetic material can keep its magnetization to some extent in a given direction after removal of the external magnetic field. This property is displayed by a magnetic hysteresis loop (M - H loop).

A typical M - H loop is shown in Fig. 2, which describes the change of the magnetization (M) of a ferromagnetic material with the variation of the intensity of an external magnetic field (H). If the initial magnetic state of a material is never magnetized or fully demagnetized ($M = 0$), the

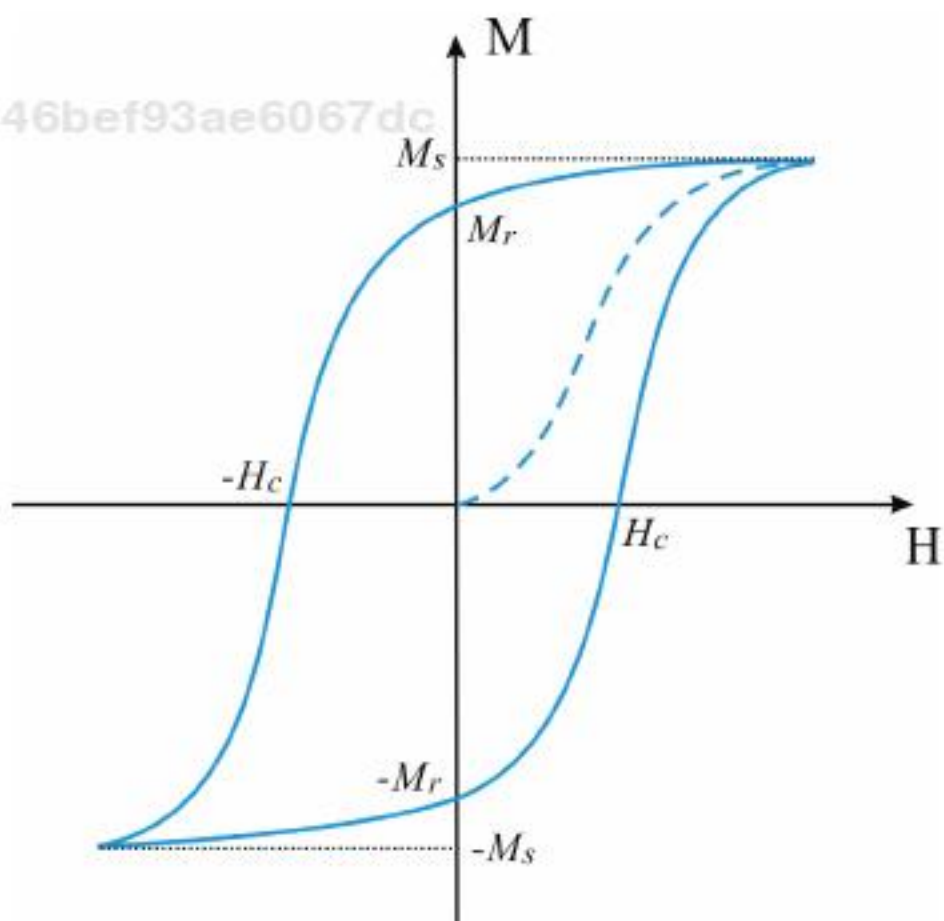


Fig. 2. A typical M - H loop for a ferromagnetic material.

5f21ac93d18f02ae446bef93ae6067dc
ebrary

magnetization will increase with increase of H , following the dashed line (called the initial magnetization curve). The maximum value of M is M_s (called saturation magnetization). At this point, all magnetic moments in the material are aligned and the material is magnetized to saturation. When H drops to zero, M will follow the solid line and have a little decrease. At the point where the external field is zero ($H = 0$), some magnetization will still remain in the material. This is called remnant magnetization (M_r), which is very important for magnetic memory devices. Then H goes to the opposite direction, and the magnetization will keep decreasing until it reaches zero. The external force required to remove all of the remnant magnetization from the material is called the coercive force, or coercivity ($-H_c$). After this point, H continues to increase in the negative direction, and magnetization in the opposite direction will be generated until it reaches another magnetic saturation ($-M_s$). Then H reduces to zero, and the magnetization will decrease to another remnant magnetization ($-M_r$). When H increases to H_c in the positive direction, the magnetization of the material will be removed again. After that, if H keeps increasing, the curve will take a different path (the solid line) to the saturation point to complete the loop. Generally, the M - H loop of a magnetic material is symmetrical relative to the center origin point O, i.e. the absolute values of M_r , M_s and H_c in both the positive and the opposite direction are the same.

As mentioned above, the M - H loop is characterized by remnant magnetization (M_r), saturation magnetization (M_s) and coercivity (H_c), which are all crucial magnetic properties of a material. M_r is the remaining magnetization of a ferromagnetic material when the applied magnetic field is removed. M_s is the maximum magnetization that a material could generate. Both M_r and M_s are dependent on the composition of the magnetic material and the processing, such as the nature of the atoms and electron structures of materials and also the crystal structures. H_c is the intensity of the external field required to remove all the magnetization of a material after saturation. Rotation and domain wall motion are two primary processes of magnetization reversal. The value of H_c is determined by these processes.⁵ Magnetic materials with $H_c < 10$ Oe are usually called soft materials; if $H_c > 100$ Oe, called hard magnetic materials. Since high H_c means that the materials are hard to demagnetize (good stability), high H_c magnetic materials are naturally used as magnetic

recording media. On the contrary, low H_c magnetic materials are good candidates for the recording head, because it is easy to reverse the magnetization by external field.

Besides, the M - H loop also provides a great deal of other information about magnets. The shape of the initial magnetization curves displays the magnetic characteristics of materials. The curve also shows the processes of domain wall motions. There are two different modes of domain wall motions: nucleation and pinning.⁶ In the nucleation-type, magnetic saturation is reached quickly at a low field. This shows that the domain wall can be easily moved and not pinned significantly. In the pinning-type, the saturation magnetization is reached only when a strong field is applied. Here domain wall is substantially pinned and a relatively strong field is needed to remove pinning sites.

Remnant squareness (S) and coercive squareness (S^*) are used to measure how square the loop is.

$$S = \frac{M_r}{M_s}, \quad S^* = 1 - \left. \frac{M_r/H_c}{\frac{dM(H)}{dH}} \right|_{H_c}.$$

Usually, large S and S^* are required for magnetic recording media since the parameter S characterizes the flux available for reading and the parameter S^* characterizes the ability of the medium to sustain sharp transition.^{7,8}

2.3. Magnetic anisotropy

The magnetization of magnetic materials always exhibits direction-dependence. This is called magnetic anisotropy, which comes from the different internal energies of the magnetization of a material in different directions. The direction, where the lowest field is required to reach the saturation magnetization is the easy axis. The direction where the highest magnetic field is required is the hard axis. Magnetic anisotropy has a strong effect on the properties of magnetic materials, such as coercivity and remnant magnetization. Therefore it is essential in the design of commercial devices based on magnetic materials.

Generally, magnetic anisotropy is influenced by the structure and symmetry of a material, known as magnetocrystalline anisotropy, which is

generated by the coupling between the electron orbital and the lattice (spin orbit coupling). Thus magnetization will be coupled to electron orbitals, resulting in the lowest or highest energy state along certain symmetry axes.¹ This can be easily determined from the different magnetization curves along different directions. For example, for a single crystal hexagonal closed-packed (hcp) cobalt, the magnetization along the [0001] direction (i.e. the *c*-axis) is much easier than along other directions; while in the basal plane ($\langle 10\bar{1}0 \rangle$, 90° from the easy direction) the magnetization is much more difficult. So the *c*-axis is the easy axis and the $\langle 10\bar{1}0 \rangle$ type directions are the hard axis.⁹ The energy required to deflect the magnetization from the magnetocrystalline easy axis to other directions is called magnetocrystalline anisotropy energy.

Also, magnetic anisotropy can be related to the mechanical stress in the system and the external magnetic field. This effect is known as magnetostriction, defined by the change of physical dimensions of materials in response to the magnetization change. The process is dominated by the migration of domain walls and the rotation of domains within the material in response to an external field, which in turn causes the change of dimensions.⁸ The inverse effect is the change of magnetization of a material when it is subjected to a mechanical stress. One example of magnetostriction application is that the easy axis of the face-centered tetragonal (fct) FePt nanoparticle can be expected to align after annealing in the presence of a magnetic field.¹⁰

The shape of magnetic grains is the third factor that affect the magnetic anisotropy. At the surface of a magnetized material, there are magnetic charges or poles, and a demagnetizing field forms in an opposite direction to the original magnetization. The magnitude of the demagnetizing field is related to the shape of the grain, resulting in the shape anisotropy. For example, considering a long needle-shaped grain, the demagnetizing field is weaker along the long axis than that along the other directions. So the magnetization easy axis is along the long axis of the grain.

2.4. Temperature dependence

The hysteresis curve mentioned above measures the magnetization of a magnetic material by varying the applied field. From the curve, a lot of

important information about the system can be obtained. Besides the hysteresis curve, the variation of temperature can also provide other important information. Temperature affects the thermal motion of atoms, which leads to the disruption of the alignment of molecular magnetic moments.

2.4.1. Curie's law

The dependence of the magnetic moment on temperature for paramagnetic materials is known as Curie's law:

$$\chi = \frac{M}{H} = \frac{C}{T}$$

Here χ is the magnetic susceptibility, M the resulting magnetization, H the applied magnetic field, C a material-specific Curie constant, and T is the absolute temperature in Kelvin. The Curie constant can be determined through experiments by plotting a χ vs. $1/T$ curve. Curie's law is valid only for materials whose magnetic moment is localized at the atomic or ionic sites and where there is no interaction between neighboring magnetic moments. This law indicates that the paramagnetic susceptibility decreases as temperature increases.

2.4.2. Curie–Weiss law

For paramagnetic materials, the relationship between magnetic moment and temperature can be described by Curie's law. The Curie constant C is the slope of the line, which is proportional to the effective magnetic moment for paramagnets. However, the law will not be valid when intermolecular interactions, such as ferromagnets, are involved. In such a system, the susceptibility obeys the Curie–Weiss law:

$$\chi = \frac{C}{T - \theta}.$$

Here θ is the Weiss constant. When $\theta = 0$, the Curie–Weiss law becomes the Curie's law. When $\theta \neq 0$, the magnitude of θ indicates the strength of

the intermolecular interaction among neighboring magnetic moments. If θ is positive, the material is ferromagnetic when the temperature is below the transition temperature (called the Curie temperature, T_C , which is equal to θ); if θ is negative, the material is antiferromagnetic when the temperature is below the transition temperature (called the Néel temperature, T_N). The Curie temperature is important in magnetic recording, which indicates on the energy required to disrupt the long range magnetization ordering in the material.

2.4.3. Van Vleck's equation

The total magnetic moment of electron is composed of both spin magnetic moment S and orbital magnetic moment L . Typically, only spin is considered since the spin moment is much greater than the orbital moment like transition metal ions: high spin Mn^{2+} or Fe^{3+} ; Ni^{2+} , Cr^{3+} or Mn^{4+} in an octahedral field; Cu^{2+} and Mn^{3+} as Jahn–Teller distortion.¹¹ However, for some other ions, such as octahedral Co^{2+} , the orbital contribution is significant to the magnetic moment. In that case, Van Vleck's equation is applied.

To derive the equation, the energy term can be expressed as a power series of the applied field (H_0):

$$E_n = E_n^{(0)} + E_n^{(1)}H_0 + E_n^{(2)}H_0^2 + \dots$$

5f21ac93d18f02ae446bef93ae6067dc

ebrary Here $E_n^{(0)}$ is the energy of state n when $H_0 = 0$; $E_n^{(1)}$ is the first order Zeeman coefficient (a measure of change in the energy of state n due to interaction with H_0); $E_n^{(2)}$ is the second order Zeeman coefficient (a measure of change in the energy of state n due to field-induced interaction of state n with higher energy states). After several approximations, the magnetic susceptibility can be described as:

$$\chi = N \frac{\sum_n \left[\frac{(E_n^{(1)})^2}{kT} - 2E_n^{(2)} \right] \exp\left(\frac{-E_n^{(0)}}{kT}\right)}{\sum_n \exp\left(\frac{-E_n^{(0)}}{kT}\right)}.$$

5f21ac93d18f02ae446bef93ae6067dc

ebrary

From this equation, the magnetic susceptibility is determined by taking a population-weighted average of the specific level susceptibility. (Van Vleck's work^{12,13} is recommended for further reading.)

3. Conventional Magnetic Storage Technology and Its Challenge

In current magnetic hard disk drives (HDDs), longitudinal recording is employed as the basic method. In this recording mode, the magnetization of recorded bits is parallel to the surface of the disk, as shown in Fig. 3. The recording head moves over the medium at a small fly height. Nowadays, the performance of longitudinal recording has been improved by the giant magnetoresistive (GMR) head. The new recording head consists of separate reading and writing elements, which can be optimized individually. Using the inductive ring type write head can record data along a track with either positive or negative direction in the medium. The resulting stray field pattern is read back by a GMR reading sensor that is located in a narrow gap between two magnetic shields. The shields are used to decrease the interference of the undesired magnetic fields generated from the medium. GMR sensor can therefore "read" only the magnetic field from the desired data bit.¹⁴

The GMR effect can be explained by the interaction of electron spin and magnetic field. It is well known that an electron can either spin up or spin down. If the spin direction of conduction electrons is parallel to the

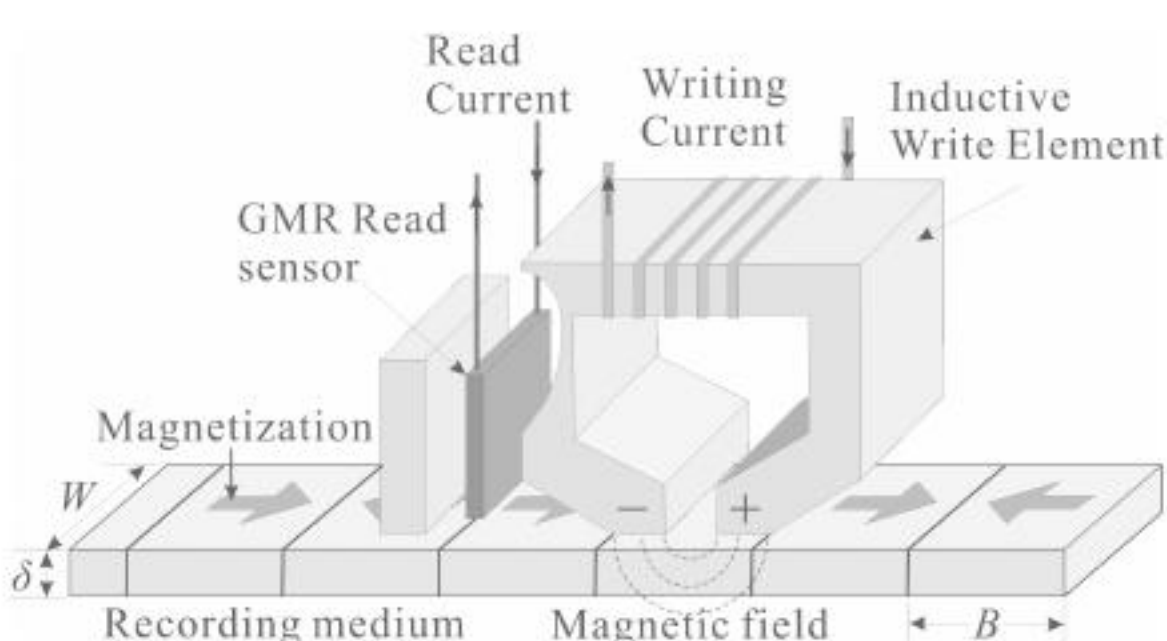


Fig. 3. A typical longitudinal recording model. δ is the medium thickness, W is the track width and B is the bit length. (Adapted from Ref. 9 with permission, © 2000, IBM)

magnetic orientation of the material, it will move with less resistance. On the contrary, if the spin direction of conduction electrons is opposite to the magnetic orientation, it will collide with atoms frequently, resulting in a high resistance. This phenomenon is called the GMR effect, which was first discovered in the Fe/Cr multilayer¹⁵ and later also found in other inhomogeneous materials, such as the Co/Cu multilayer.¹⁶

The application of the GMR effect led to a new development — the spin-valve read head, with a multilayer structure. Generally, it consists of the following layers. The first is an antiferromagnetic exchange film (e.g. FeMn). It is used to “pin” the Co layer magnetization in a certain direction. The ferromagnetic Co layer is called a pinned layer. Next is a copper spacer layer, followed by the second ferromagnetic layer, called a free layer. Typically CoFe or NiFe is used as a free layer because it is magnetically soft and can be aligned parallel or antiparallel by very small fields. Finally, there is an underlayer (e.g. Ta), which gives a good surface to grow on and a cap to avoid oxidization in air.¹⁷ The exchange coupling between the two ferromagnetic layers can be mediated by conduction electrons in the spacer layer. When a strong external field is applied, the direction of the magnetization in both magnetic layers will be aligned, from an antiparallel to a parallel configuration, which will exhibit a distinct change in resistance, with a concomitant change in current (for a constant applied voltage). For the Fe/Cr multilayer, the experiment demonstrated that the change of resistance is more than 50%.¹⁵ (For the physical description of GMR, please check Ref. 7.)

The discovery and application of the GMR effect in the read head improved the ability to sense a change in the magnetic field that occurs within a very small distance. Thus the GMR read head can detect small recorded bits and read them at higher data rate. It creates more room to reduce the size of bits and increase the areal density of magnetic recording. However, the optimization of the areal density is still limited by the material of the recording media.

As the candidate of magnetic recording media, several aspects must be considered: high signal-to-noise ratio (SNR), high thermal stability, very smooth surface and small magnetic grains with uniform size. The most common one is a thin film medium, with complex multilayers. The structure, material and function of each layer are shown in Table 1. Underlayer

Table 1. Schematic illustration of the layer structure, material and function of thin film used for longitudinal magnetic recording.^{21,22}

Layer structure	Material	Function
Lubricant	Perfluoropolyether	Lubrication
Overcoat	Carbon	Protection
Magnetic layer	Co alloy	Recording
Underlayer	Chromium (Cr)	Orientation control
Sublayer	NiP	Hardness
Substrate	AlMg/glass	

5f21ac93d18f02ae446bef93ae6067dc
ebrary

can promote the growth of a particular crystallographic texture, grain size and morphology in the magnetic layer. As a result, it increases the coercivity and squareness of the magnetic layer. Because of the similar atomic orientation and size relationships between hcp Co grains and bcc Cr grains, Co alloy films can grow with a significant degree of heteroepitaxy on the Cr underlayer.¹⁸ The crystallographic texture of Co alloy can be controlled by modifying the microstructure of the Cr underlayer, which depends on growth process conditions, such as the base vacuum, the temperature of the substrate, the pressure of the sputter gas and the film thickness.¹⁹ Besides the Cr underlayer, NiAl is used as an alternative underlayer because it produces finer grains in the magnetic layer.²⁰ The carbon overcoat is used to protect the magnetic film from mechanical damage and corrosion during the start and stop point of the reading and writing processes. A layer of NiP, deposited on the substrate, is used to enhance the durability of the combined film structure.

The magnetic layer is essential in the recording system. The requirements for hard magnetic media to obtain very sharp transitions and high readback signal are the following: high remnant magnetization (M_r), saturation magnetization (M_s), coercivity (H_c), magnetic anisotropy, and small thickness (δ).²¹ So far, several materials have been selected as magnetic recording media, such as $\gamma\text{-Fe}_2\text{O}_3$, Co alloy,²³ CrO_2 and barium ferrite.

To obtain a high areal density, one employs the scaling method by shrinking the relevant head and medium dimension (including bit

5f21ac93d18f02ae446bef93ae6067dc
ebrary

length, track width, medium grain size, medium thickness, fly height and head gap) by a factor s , which causes an increase of areal density by s^2 . However, this approach cannot continue indefinitely, for several reasons. First, current technologies are unable to achieve such dimensions. Second, the scaling will lose the amplitude of the signal and decrease the SNR rapidly, which has to be compensated for by a more sensitive reading head design. Third, when the size is smaller than a critical value, the electronic and magnetic properties of the grain will change dramatically. Moreover, when the distance between the head and the medium becomes too short, the tunneling effect and surface roughness will have to be considered. Finally, in recording bits, if the size of the grain is too small, the medium will no longer be thermally stable and data loss will occur. The distribution of grain size affects areal density. If the size is not uniform, but spreads in a range, the information stored in smaller ones will decay more quickly than that in larger ones. Therefore, decreasing the distribution of grain size will improve the SNR. An ideal magnetic medium should contain small grains with a narrow distribution of the size.

According to the physics of magnetics, two key factors must be considered in order to achieve very high areal density: (1) the superparamagnetic effect (thermal stability) in recording media; (2) the finite sensitivity of the readback head. In both cases, the limitation arises because the signal energy becomes too small to be comparable with the ambient thermal energy.²⁴

Thermal stability sets an upper limit on the areal density of the medium in magnetic recording. The Arrhenius equation indicates the relationship between the relaxation time τ and the activation energy barrier of magnetization reversal E_B :^{23,25}

$$\tau_{\pm} = \tau_0 \exp\left(\frac{E_B^{\pm}}{k_B T}\right).$$

In the absence of an external field H , $E_B^0 = K_u V$, where K_u is the magnetic anisotropy and V is the volume of grains, + and – mean the “upward” and the “downward” magnetization direction respectively, and τ_0 is

the characteristic relaxation time, determined by the intrinsic properties of the recording medium. When the grain gets smaller, the energy barrier in each grain ($K_u V$) becomes so close to the thermal energy ($k_B T$, where k_B is Boltzmann's constant and T is the temperature) that the releasing time decreases dramatically. This is known as the superparamagnetic effect. With the presence of external magnetic field H ,

$$E_B^\pm(H, V) = E_B^0 \left(1 \mp \frac{H}{H_0} \right)^n, \quad E_B \text{ can be either increased or decreased and}$$

the thermal decay will be affected. Here, H_0 is the intrinsic switching field. Generally, in order to avoid thermal instability, $K_u V/k_B T \approx 50\text{--}70$ is required for magnetic media.^{3,23} Several improvements have been tested to increase thermal stability by improving epitaxy²⁶ and perfecting the magnetocrystalline,^{24,27} or using magnetic materials with ultrahigh magnetic anisotropy such as hexagonal close-packed phase CoPt oxide media with high Pt content, L1₀ phase-ordered CoPt and FePt alloys, or (Co/Pd)_n multilayer structures.^{27,28} However, because of the constraint of the writing head, the infinitely high K_u material is not reasonable.

To increase the sensitivity of the reading head, alternatives must be explored to improve areal density. The tunneling magnetoresistance (TMR) sensor may be applied in the future; it consists of an antiferromagnetic layer, a reference layer, a tunneling barrier and a free layer.²⁹ The challenge of applying it in recording systems is to obtain efficiently small resistance. Since the resistance of a tunneling junction increases exponentially with the thickness of the oxide tunneling barrier (e.g. a normal aluminum oxide monolayer), the barrier thickness must be uniform at the atomic level. This presents a huge technical challenge.

In order to accomplish ultrahigh density data recording, the longitudinal recording mode requires an infinitely thin recording layer combined with an excessively high coercive force. However, the former implies a deterioration of the SNR due to a drastic reduction of the reading flux from the medium, and the latter is limited by the writing ability of the inductive write head. In practice, these factors place an upper limit on the areal density. Therefore, this becomes an obstacle to realizing ultrahigh density longitudinal recording.

4. High Density Magnetic Recording

As discussed above, the areal density of the conventional longitudinal recording model is limited by the superparamagnetic effect. New approaches are needed to fulfill the requirements of the rapid growth rate of information. Perpendicular recording is technically the closest alternative to longitudinal recording, in which the magnetization of recorded bits is normal to the plane of the medium. It saves space and increases thermal stability. Patterned media (the location and size of the magnetic features are predetermined by the medium manufacturing process) are used with one grain as one bit, so the capacity is increased. To get even smaller patterned uniform grains, self-assembled magnetic nanoparticle arrays are the most promising method due to their low cost and large area. Besides conventional magnetic materials, new materials are explored. Molecular-based magnets give more room for further increase of areal density data storage.

4.1. *Perpendicular recording*

The perpendicular recording technology was proposed by Prof. Iwasaki in 1975.^{30,31} It is a promising candidate for high density magnetic data storage, since it is technically the closest to conventional longitudinal compared with other technologies and methods. The significant difference between perpendicular and longitudinal recording is that the former orients the magnetization of the recording bit normal to the surface of the medium, thereby saving space in the plane of the medium and increasing thermal stability. Using perpendicular recording technology, an areal density of 345 Gbits/in² was achieved in laboratory demonstration.² Since the maximum areal density achievable by perpendicular recording is expected to be beyond 1 Tb/in²,³² there is room for further improvement. The following discusses the special design of the recording head, media and advantages and challenges of perpendicular recording. Detailed reviews can be found in Refs. 28, 33 and 34.

The typical perpendicular recording model is shown in Fig. 4. There are three key elements in perpendicular recording: a single pole perpendicular write head,³¹ a CoCr anisotropy recording film³⁵ and a soft magnetic underlayer (SUL).³⁶

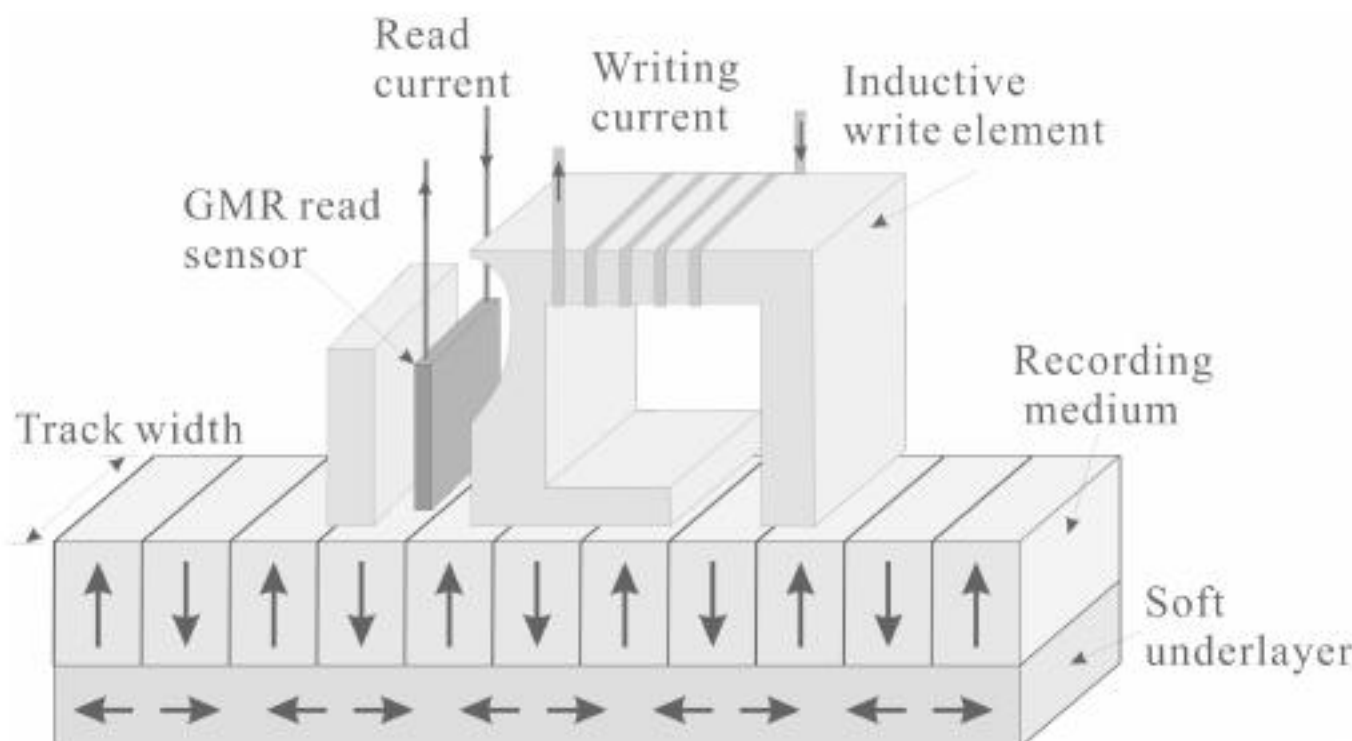


Fig. 4. A typical perpendicular recording model: a magnetic recording medium and a soft underlayer used together with a single-pole head. (Adapted from Ref. 9 with permission, © 2000, IBM)

4.1.1. Single pole write head

In conventional longitudinal recording, the maximum field generated from a ring head (RH) is limited by $2\pi M_s$, where M_s is the saturation magnetization of the write-pole material while in perpendicular recording the write field is generated between the trail pole of a single pole head and a soft underlayer. In this geometry, the upper limit of the write field is $4\pi M_s$, twice the field from the longitudinal recording head. The ability to generate higher fields makes it feasible to record bits on a higher magnetic anisotropy medium, which in turn further delays the superparamagnetic limit to a higher areal density.³⁷ Thereby, to realize higher-resolution writing, a strong and sharp perpendicular field from a single pole type write head is required.^{38–40} This requires that a single pole write head should be designed to energize the recording medium. A recording layer should consist of a single pole head and a double-layered medium. Also, a soft magnetic back-layer is designed to effectively bring out the effect of magneto static interaction between them. Besides, the recording layer of the medium should be made to narrow the dispersion of the grain size and coercivity.

4.1.2. Perpendicular recording media

Perpendicular recording provides a new technique to postpone the limitation of thermal stability. One of the important reasons in the

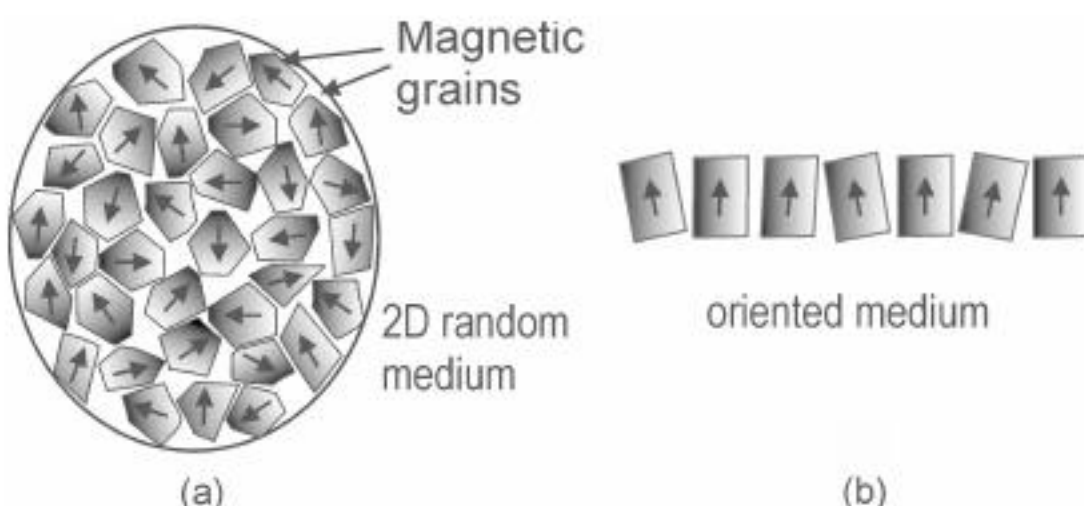


Fig. 5. Schematic diagrams illustrating (a) a longitudinal medium with randomly oriented easy axes and (b) a perpendicular medium with aligned easy axes. (Adapted with permission from Ref. 42, © 2004, Kluwer Academic Publishers)

perpendicular recording mode is the relatively well-aligned easy axis of each magnetic grain in the direction perpendicular to the plane of the disk [see Fig. 5(b)]. Thus, the bit transition in such a highly aligned film relaxes the stringent requirements of the write field for achieving sharp transitions for conventional longitudinal recording, where the magnetization is randomly oriented in the plane [see Fig. 5(a)].^{41,42} Also, the opposite states of magnetization in neighboring bits generate a minimum demagnetization field, making the bits smaller without superparamagnetism and keeping their memory. Since the demagnetization field in perpendicular recording decreases with increasing thickness, thicker media with smaller grain can be applied in perpendicular recording than in longitudinal recording to achieve the same areal density.

An ideal perpendicular recording medium requires:

- (1) Sufficiently small and uniform grains with a small intragranular exchange to increase the SNR
- (2) A high anisotropy and texture control to improve thermal stability
- (3) Unity squareness ($S \approx 1$) of its $M-H$ loop to avoid excess noise in the DC saturated state.

The typical perpendicular recording medium has a double-layered structure composed of a magnetic recording layer (a hard magnetic material with high magnetic anisotropy) and a soft underlayer (a soft magnetic material). The latter is a new component compared with the longitudinal recording model. Its function will be discussed later.

To optimize the specifics, the materials with high magnetic anisotropy are used as magnetic recording layers. So far, two types⁴¹ of recording magnetic materials have been used in the perpendicular recording model:

- (1) Alloy-based media, such as CoCr alloy,³⁵ L1₀ phase FePt⁴³ and CoPt. The magnetic anisotropy is controlled by the magnetocrystalline anisotropy, so it is highly textured.
- (2) Multilayer-based magnetic media, such as CoCr/Pt,⁴⁴ and Co/Pd⁴⁵ multilayered films. The magnetic anisotropy is controlled by the interfacial interaction between a magnetic layer (such as Co) and a high polarization nonmagnetic spacer (such as Pd or Pt). This type of media is weakly textured.

Comparing those two kinds of recording magnetic layers, the latter is preferable because it has a significantly larger anisotropy and a remnant squareness of one. Consequently, the anisotropy field, H_k , which keeps the magnetization in the perpendicular-to-the-disk direction, is larger than the maximum demagnetizing field, $4\pi M_s$. Therefore, the thermal stability can be improved and a higher areal density can be achieved.

4.1.3. *Soft underlayer (SUL)*

The use of the SUL, located below the recording layer, is a critical part of perpendicular magnetic recording. It provides the possibility of recording on media with high anisotropy, which increases the thermal stability of the recorded information in the disk. The effect of the SUL is like a mirror in both the write and the read process. It directs the magnetic flux from the write pole to the collector pole and generates a mirror image of the write pole. This results in almost doubling of the write field and reducing the demagnetizing field, thus recording bits at a higher density than conventional longitudinal recording.

The characteristics of the longitudinal and perpendicular recording models are summarized in Table 2.^{46,47} Perpendicular recording is considered as the promising alternative to conventional longitudinal magnetic recording technology. The highly aligned anisotropy axis of individual grains in perpendicular recording media facilitates recording narrow

Table 2. Complementarity between the longitudinal and perpendicular recording model. (Reprinted with permission from Ref. 47, © 2005, Elsevier)

	(a) Longitudinal model	(b) Perpendicular model
	$\lambda \rightarrow 0, H_d \rightarrow 4\pi M$	$\lambda \rightarrow 0, H_d \rightarrow 0$
Head	Dipole (ring) type	Single pole type
Medium	Longitudinal anisotropy (2D random) Thin δ Low M_s , high H_e Low squareness Recording layer only	Perpendicular anisotropy (uniaxial) Thick δ High M_s , high H_e High squareness Soft underlayer
Thermal stability	Good at low density	Good at high density
Write	Medium outside of write flux path • Narrow spacing required	Medium in write flux path • Efficient writing • High frequency writing • Wide temperature range • Relaxed spacing; sharp transition/narrow erase band • High TPI servo writing
Read	Low output • High head sensitivity required; flux from head-on transition • Wide reading	High output • High SNR • Good tracking servo • Relaxed head sensitivity; flux from coupled transition • Narrow reading

tracks with sharp transitions into a thicker recording layer, reducing noise and increasing readback signal. Moreover, the use of a soft underlayer helps to stabilize the grain. The mirror effect of the SUL produces a double writing field, which allows writing transitions in recording media with higher anisotropy, resulting in more thermal stability.

However, before perpendicular recording can be extensively applied, efforts need to make to resolve technical problems. For example, to overcome the high sensitivity of the SNR to the switching field distribution in perpendicular media, tilted media were proposed^{48,49}; to optimize head

design, heat-assisted magnetic recording (HAMR) and/or thermally assisted magnetic recording were used.⁵⁰ Perpendicular recording defers the superparamagnetic limit in the conventional longitudinal recording system, but still cannot meet the growing requirement of data storage. Further increasing the areal density will be realized by new designs and pathways. The following lists some new designs on the recording media, which are believed as promising candidates for the future data storage.

4.2. Patterned media

In conventional longitudinal magnetic recording media [as shown schematically in Fig. 6(a)], each bit contains 50–1000 grains to control the SNR. And the size of each grain is limited by thermal instability of the thin film medium. Assuming that the grain is about 10 nm (typically, a little larger), the size of a single bit will be 0.5–10 μm in size, corresponding to

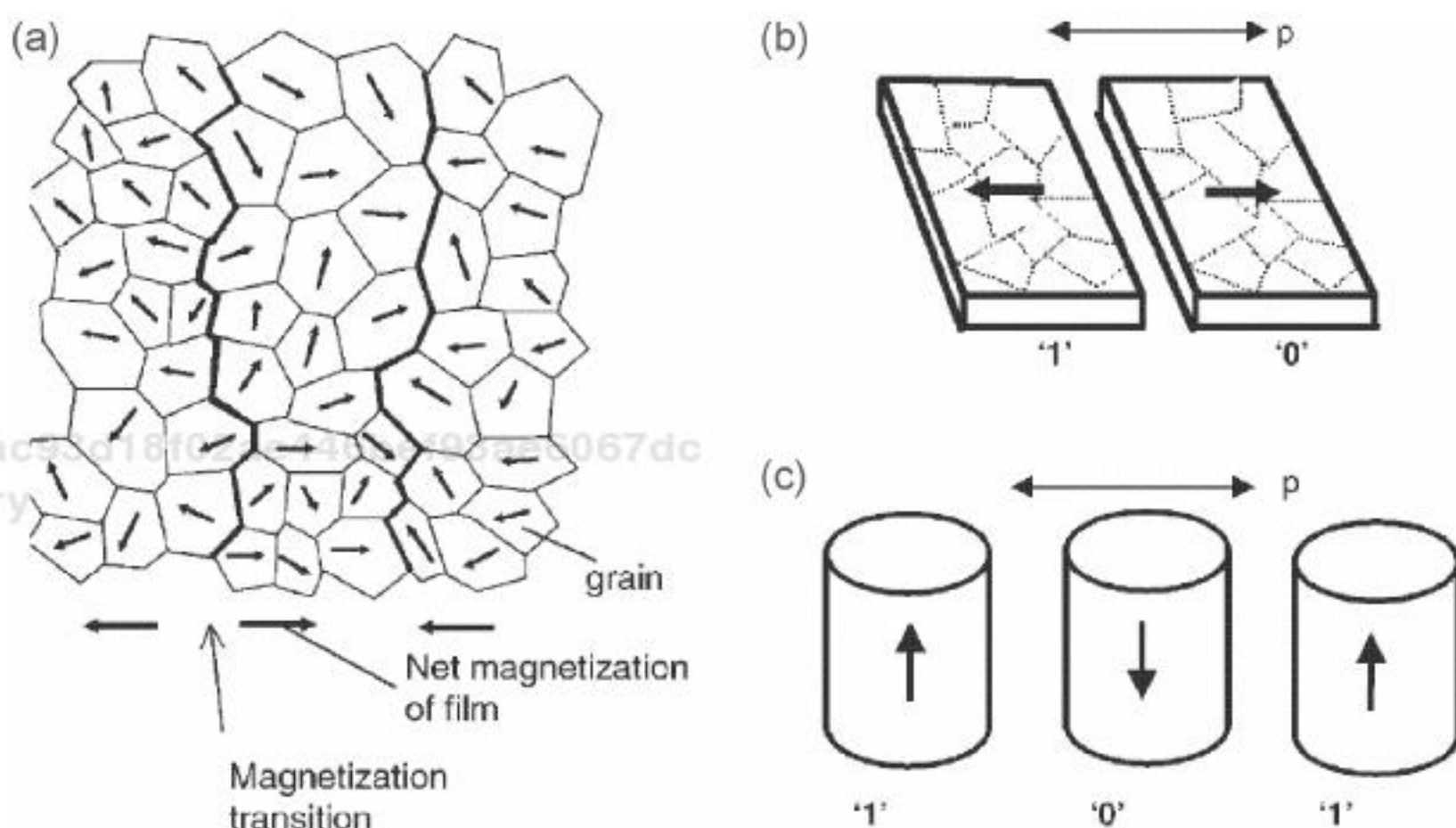


Fig. 6. Schematic drawing of (a) a conventional thin film medium, consisting of single-domain, exchange-decoupled grains. Bits are represented by the transitions between oppositely magnetized regions. Each bit cell contains tens or hundreds of grains. (b) A patterned medium with in-plane magnetization. The single-domain bits are defined lithographically with period p . They can be polycrystalline (indicated by dotted lines) with exchange coupling, or single crystal. (c) A patterned medium with perpendicular magnetization. Binaries 1 and 0 are shown. (Reprinted with permission from Ref. 51, © 2000, Annual Reviews)

an areal density of less than 15 Gbit/in². The simulation predicted that the superparamagnetic limit for longitudinal recording on thin films occurring at the densities is about 200 Gbit/in².^{3,4}

One solution to this problem is patterned magnetic media [as shown in Figs. 6(b) and 6(c)], in which data are recorded in an ordered array of highly uniform magnetic islands separated by a nonmagnetic matrix or material with altered magnets. Each island (also called the switching volume) is capable of storing an individual bit, depending on the direction of magnetization. For example, magnetization up represents “1,” and magnetization down represents “0”.⁵¹ Unlike thin film media, this island may contain one grain, or several exchange coupled grains, and each island behaves as a single magnetic domain. This may effectively eliminate the transition noise and statistical noise problems.^{23,52} Moreover, the transitions are now defined by the patterning and not by the head field. Thus, patterned media are much more stable than the conventional recording media; even those islands are smaller than 10 nm. As a result, the areal density can be increased dramatically compared to conventional recording media. For example, a 50-nm-period patterned medium corresponds to a density of 250 Gbit/in², and a 25-nm-period one corresponds to a density of around 1 Tbit/in².⁵³ Therefore, a patterned medium is a promising candidate for the future recording system with a capacity beyond 1 Tbit/in². However, there are a number of technical problems which need to be resolved, such as fabrication of large-area arrays of magnetic grains with size less than 50 nm at low cost, addressing of the array with high spatial precision, and different recording and writing mechanisms and systems. These issues will be discussed below.

4.2.1. *Fabrication of patterned media by lithography*

Nowadays, significant efforts are devoted to the fabrication of patterned recording media. Many methods have been reviewed to fabricate nanoscale or submicroscale patterned magnetic elements.^{51,55–57} Unfortunately, conventional photolithography no longer meets the requirement for the high resolution of patterned media. In conventional photolithography, a pattern of a geometric shape is created in a mask, and then transferred to a thin radiation-sensitive layer material (called resist), which is placed on the surface of a semiconductor wafer. Finally, the areas which are not protected

by the resist are removed through etching. The resolution in conventional photolithography is limited by the wavelength of light (λ) used and the system numerical aperture (NA) with a minimum feature size of about $\lambda/(2NA)$. For generation of highly ordered arrays of uniform “islands” with dimensions smaller than 50 nm, the conventional optical method cannot work. Instead, some advanced nanolithography techniques, such as E(electron)-beam lithography, X-ray lithography, nanoimprint lithography and interferometric lithography, need to be used.

Among the aforementioned nanolithography techniques, E-beam lithography is widely used to fabricate patterned media. Here, an electron beam is used to write a desired structure directly on a thin resist layer. Although the calculation from diffraction limitation predicts that an E-beam lithography can be obtained as a spot as small as 1 nm by increasing the energy of the electron beam, the secondary electrons produced by high energy electrons⁵⁸ and the following process⁵⁷ limit its resolution. Theoretically, 10 nm spots are possible, and so far the smallest spot demonstrated is an array of 12 nm dots with a 25 nm period by E-beam lithography on a AuPt layer,⁵³ which suggests a potential density of around 1 Tbit/in² for patterned bits. Compared to other methods, E-beam lithography has high resolution, excellent flexibility and reasonable patterning speed. Due to low throughput and expense, when exposing large areas, stitching errors between the different written fields will distort the long range coherence of the array. Therefore, this method is not suitable for the fabrication of large-area samples.⁵¹ However, E-beam lithography can be applied for preparation of masks for master/replication methods, such as nanoimprinting.

In X-ray lithography, UV light is replaced by X-rays, which are produced by synchrotron radiation from a bending magnet in a high energy electron storage ring. The advantage of using X-rays is that diffraction effects can be reduced significantly because the wavelength of X-rays (0.4–5 nm) is much shorter than that of UV light (200–400 nm). Therefore, higher resolution can be achieved. As with high energy electron beams, X-rays have a photoelectron blur problem, which is caused by the excitation of photoelectrons and the associated shower of secondary electrons. Ultimately, this places a limit on the smallest achievable feature.⁵⁸ The resolution limit of X-ray lithography is about 20 nm. However, X-ray

lithography has a high throughput capability because parallel exposure can be adopted.⁵⁷

Nanoimprint lithography (NIL) includes two processes. One is nanoimprinting. In this process, a mold with nanometer scale features is imprinted on a thin resist film and creates a pattern with a thickness contrast in the film. The other process is ‘lithography’, which transfers the pattern into the entire resist thickness by anisotropic etching.⁵⁹ Although the mold must first be patterned by E-beam lithography or other methods which may be expensive and time-consuming, repeatable use with a long lifetime (depending only on the limit of wear and contamination) will be able to counteract this disadvantage. Therefore, this technique is inexpensive and time-saving. Moreover, the duplicating process of nanostructures on the mold in the resist film is not affected by wave scattering, diffraction and interference in a resist, and backscattering from a substrate. Therefore nanoimprint lithography provides a way to fabricate sub-10-nm structures. In the past few years, it has received considerable attention. For example, metal patterns with a feature size of 25 nm and a period of 70 nm were made with a lift-off process by nanoimprint lithography.⁶⁰

Interference lithography (IL), or holographic lithography, allows periodic arrays of identical particles to be made over several square centimeters. For two-beam interference, two coherent beams interfere at an angle 2ϕ to produce a standing wave, which is recorded in a recording layer (photoresist) with a period of $\lambda/(2 \sin\phi)$. There are also three-beam interference and four-beam interference, which can create different patterns in the photoresist. The minimum spatial period of a pattern is then half the wavelength of the interfering light. Employing UV wavelengths, 200-nm-period gratings can be obtained. For the spatial period of the order of 100 nm, a deep ultraviolet DUV ArF laser ($\lambda = 193$ nm) can be used.⁶¹ But short excimer laser generates too broad a range of wavelengths to produce sufficiently sharp interference patterns. To compensate for the diffraction limit of $\lambda/2$, an achromatic interferometer lithography (AIL) system has been developed, in which the radiation is diffracted by a set of three-phase gratings. The period of the pattern is given by half the period of the gratings, independent of the laser wavelength.^{62,63} For example, an array of a 30 nm nickel–chromium alloy with a period of 100 nm was made.⁶⁴ To further reduce the period, a new generation of the AIL system is under

development for producing 50-nm-period patterns on a substrate, or even as low as 10 nm.⁵⁴

Lastly, one more appealing method, self-assembled block copolymer lithography^{65–67} is discussed. A block copolymer polymerized from two chemically distinct monomers can microphase-separate into a monolayer of nanoscale domains.⁶⁸ Then the structure is used as a template for the following growth of magnetic patterns. The geometry of the template depends on the length of each block. For example, a PS-PFS (polystyrene/polyferrocenyldimethylsilane) copolymer was used to fabricate single domain cobalt dot arrays with the magnetic islands as small as 25 nm.⁶⁹ The approach provides a simple and controllable process for making an array of magnetic nanodots. However, the array lacks long range order. To solve this problem, templated (or guided) self-assembly^{70–73} is proposed, in which a substrate with topographical features or chemical heterogeneities^{74,75} is used to induce orientation and ordering of the self-assembled block copolymer. A 2.5-inch disk patterned medium of Co₇₄Cr₆Pt₂₀ with ~40-nm-diameter islands was prepared via a combination of graphoepitaxy and self-assembly.⁷⁶ A similar method reported for creating nanostructure is to orient a block copolymer under an applied electric field. Here, the block copolymer comprises blocks with different dielectric constants, such as a copolymer of polystyrene-polymethylmethacrylate (PS-PMMA).⁷⁷ Annealing under an applied electric field leads to a hexagonal array of PMMA cylinders oriented parallel to the direction of the field. Then, the removal of PMMA by acetic acid gives an ultrahigh density nanoporous film. By electrodeposition, nanowires with a diameter of 14 nm can grow in the porous template, which will create an ordered array of nanowires, corresponding to an areal density beyond 1 Tbit/in².

Without using a resist, the desired pattern can be directly written on the magnetic film by ion irradiation. When different ions (He⁺, Ar⁺, Ga⁺, N⁺) with varying exposure doses (fluence) interact with the surface, many effects occur. These include radiation damage, elastic reflected ions, implantation and ion etching (milling).⁵⁵ One example is the perpendicular granular CoCrPt media with an ~100 nm period and ~70 nm islands prepared by focused Ga⁺ ion beam (FIB).⁷⁸ Irradiation with light ions typically results in a patterned magnetic structure separated spatially by altered magnetic anisotropy, without changing the surface topography.

The disadvantage here is the lack of throughput and speed to meet the requirement of manufacturing patterned media. Using mask techniques, this issue might be addressed partially. Projection ion beam irradiation has been used to produce a large area of a patterned Co/Pt multilayer.^{79,80} The light ion lithography has been reviewed recently.⁸¹

Some other fabrication processes, such as the AFM (atomic force microscopy)/STM (scanning tunneling microscopy)-based probe lithography system, have been developed. They are suitable for producing small dots, but more efforts need to improve the lithography speed, reproducibility and the ability to produce large-area samples.

4.2.2. *Magnetic properties*

The fabrication is not the only problem associated with patterned media. Integrating patterned media into a disk drive presents another big challenge. When one analyzes the recording process, understanding and modeling the magnetic properties of those small particles are very important. The magnetic properties of nanostructured elements have been reviewed recently.⁵⁶ An ideal patterned medium should be composed of a thermally stable and noninteracting single domain particle with two well-defined remnant states for information storage. Besides, the switching field distribution should be narrow enough to prevent the field gradient of the write head from addressing more than one island, and the saturation magnetization should be turned to optimize recording, thermal stability and read-back signal amplitude.⁵⁷

The coercivity H_c and the remnant-to-saturation magnetization ratio M_r/M_s (also called remnant squareness, S) of magnetic particles are dependent of the size of particles,^{82,83} as shown in Fig. 7. The above two properties have maximum values when the size of particles reaches the critical value, depending on the chemical composition and crystalline structure of the particles. For instance, the critical size is 20~40 nm for the CoNi alloy system,⁸⁴ where the nanoparticles have the highest coercivities.

For polycrystalline particles, there should be exchange coupling existing inside to avoid formation of domain walls. When the size of particles is less than the critical value, single domain remnant behavior is expected. Otherwise, domain structures exist in particles and both coercivity

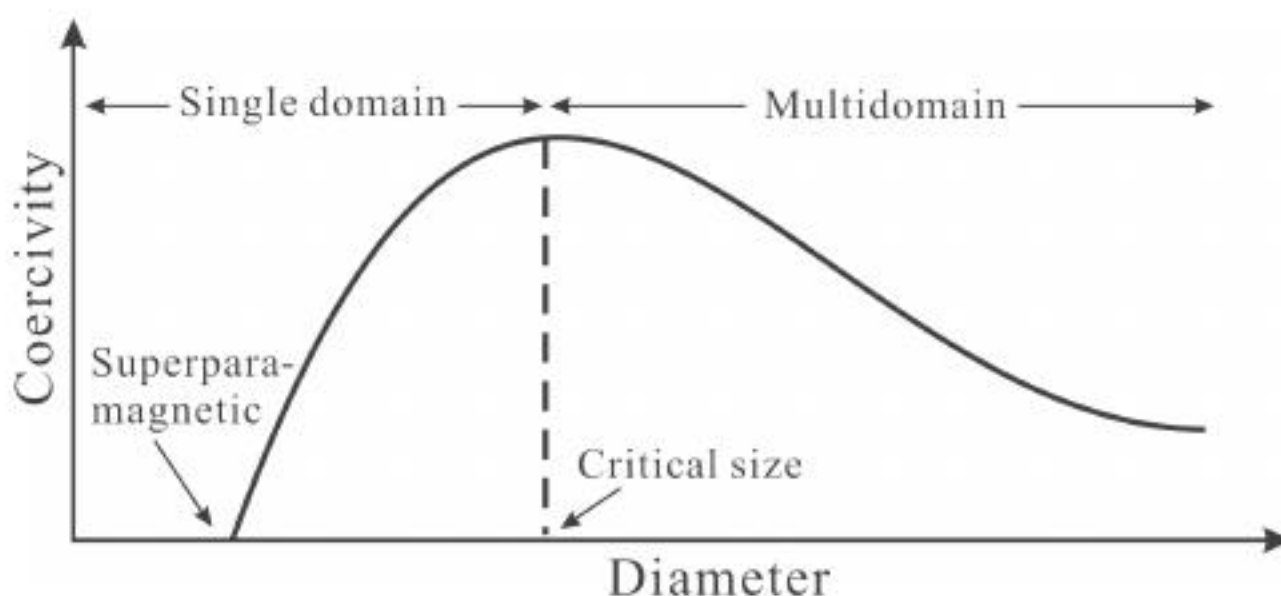


Fig. 7. Schematic curve of coercivity as a function of particle size.

and remnant magnetization of particles will be reduced. On the other hand, when particles are too small, the nanoparticles gradually become superparamagnetic due to random anisotropy. In order to obtain a high areal density for data storage, the size of particles should be within the range where the particles can be expected as a single domain, even in the presence of some defects.

Compared with continuous films, the bit size in patterned media is defined by lithography, not the read/write head. Thus, a high coercivity is not necessary, which provides a wide choice of magnetic materials. Another difference is that in patterned media the structure and shape anisotropies of islands are much more important than others. In particular, shape anisotropy determines the easy axis of magnetic nanoparticles and plays a key role in the process of magnetic reversal. Small variations in the particle's size, shape and microstructure and the magnetostatic interaction between particles lead to changes of coercivity, width of the switching field, etc. Therefore, controlling the size, shape, distribution and array of particles is crucial in the design of patterned media.

4.2.3. Recording data in patterned media

The fabrication of patterned media is not the only issue that needs to be investigated. The methods of recording data in patterned media have also been explored in the last few years. Currently, patterned media can be recorded by scanning probe microscopy (SPM) or MR head technique.

In SPM, an magnetic force microscopy (MFM) tip is used to address patterned particles. The principle of MFM is similar to that of noncontact atomic force microscopy (AFM) except that magnetic materials are used for the sample and tip. Thus, the atomic force and the magnetic interaction are both detected in MFM. Writing data can be realized through the MFM tip (if the magnetization of the tip is strong enough) or by applying an external field. The read-back process can be accomplished by detecting the magnetic states from the change in the oscillation of the cantilever that holds the magnetic tips. To improve the resolution of the writing, the tip should be very close to the patterned element, so that the magnetic field affects only one bit, not other nearby particles. To optimize the writing resolution and prevent inadvertent writing, a method of thermomagnetic writing is used, by passing a current from an MFM tip to a magnetic particle.⁸⁵ To increase the recording rate, there is a new technology called the Millipede (reported by IBM), where arrayed cantilevers are used. Each cantilever is equipped with a heater on its tip and working in parallel. Therefore, the Millipede provides a new approach to storing data at high speed and with an ultrahigh density.⁸⁶

The alternative method is the MR head technique; however, an issue encountered is how to synchronize the writing signal with the physical location of magnetic islands. So far, most experiments have been done using a quasistatic write/read tester together with MFM to study patterned media. The tester consists of a conventional longitudinal inductive write/GMR read head and a piezoelectric x-y stage, which controls the relative position of the sample of the patterned medium.⁸⁷ The synchronization requirements for writing bits in patterned media were investigated on a single row of islands.⁸⁸ The study of the recording system in both longitudinal and perpendicular Co₇₀Cr₁₈Pt₁₂ patterned media (see Fig. 8) reveals that a significant “writing window”, where islands can be written 100% correctly, is of about half the island period.⁸⁹ Quantitative analyses show that writing patterned islands correctly in longitudinal media is easier than in perpendicular media, which is consistent with the hypothesis that the window strongly depends on the field gradient of the write head and the switching field distribution (SFD) of islands. Therefore, to expand the writing window or to increase the writing performance of patterned media, narrowing the SFD and increasing the high head field gradients are required.⁸⁹

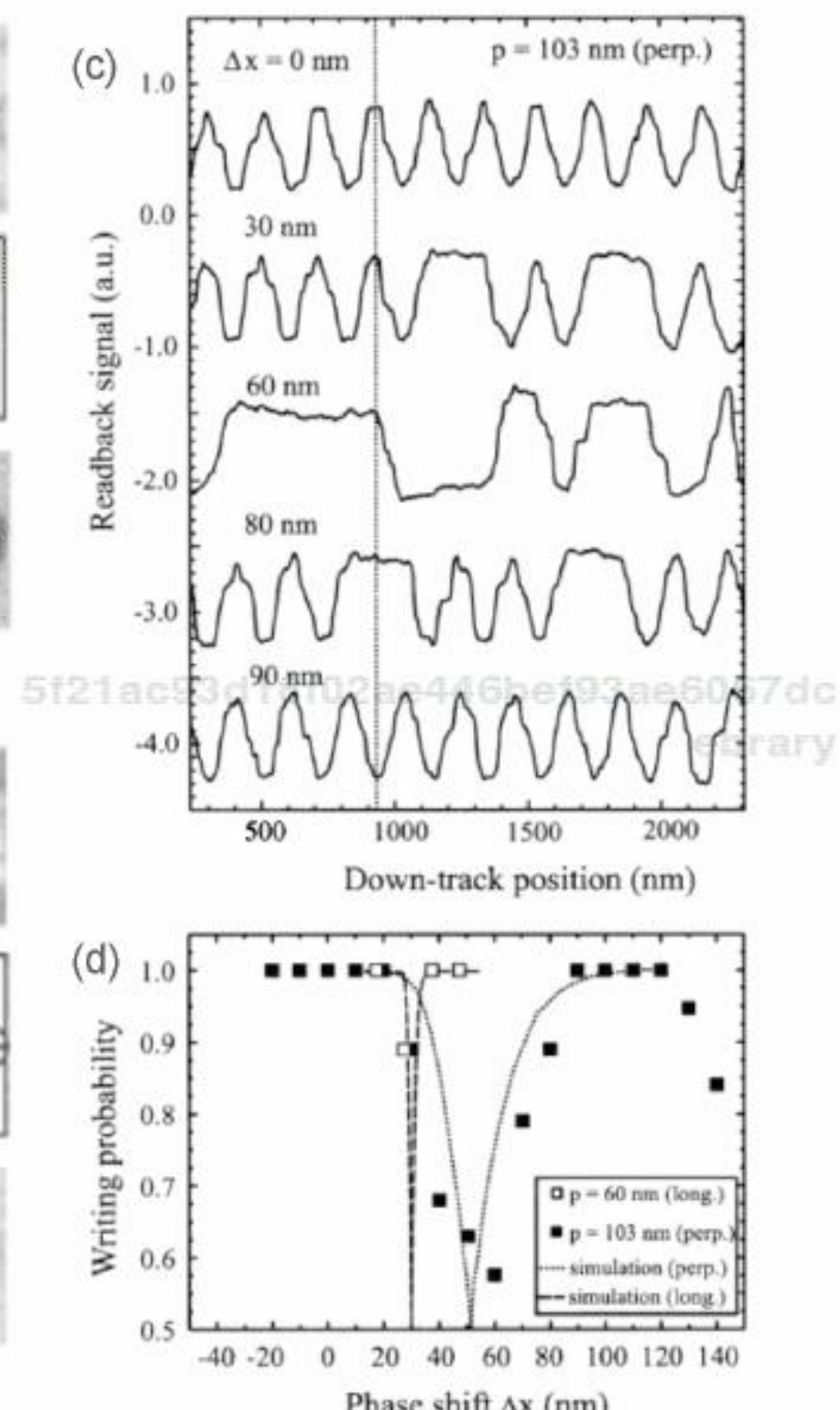
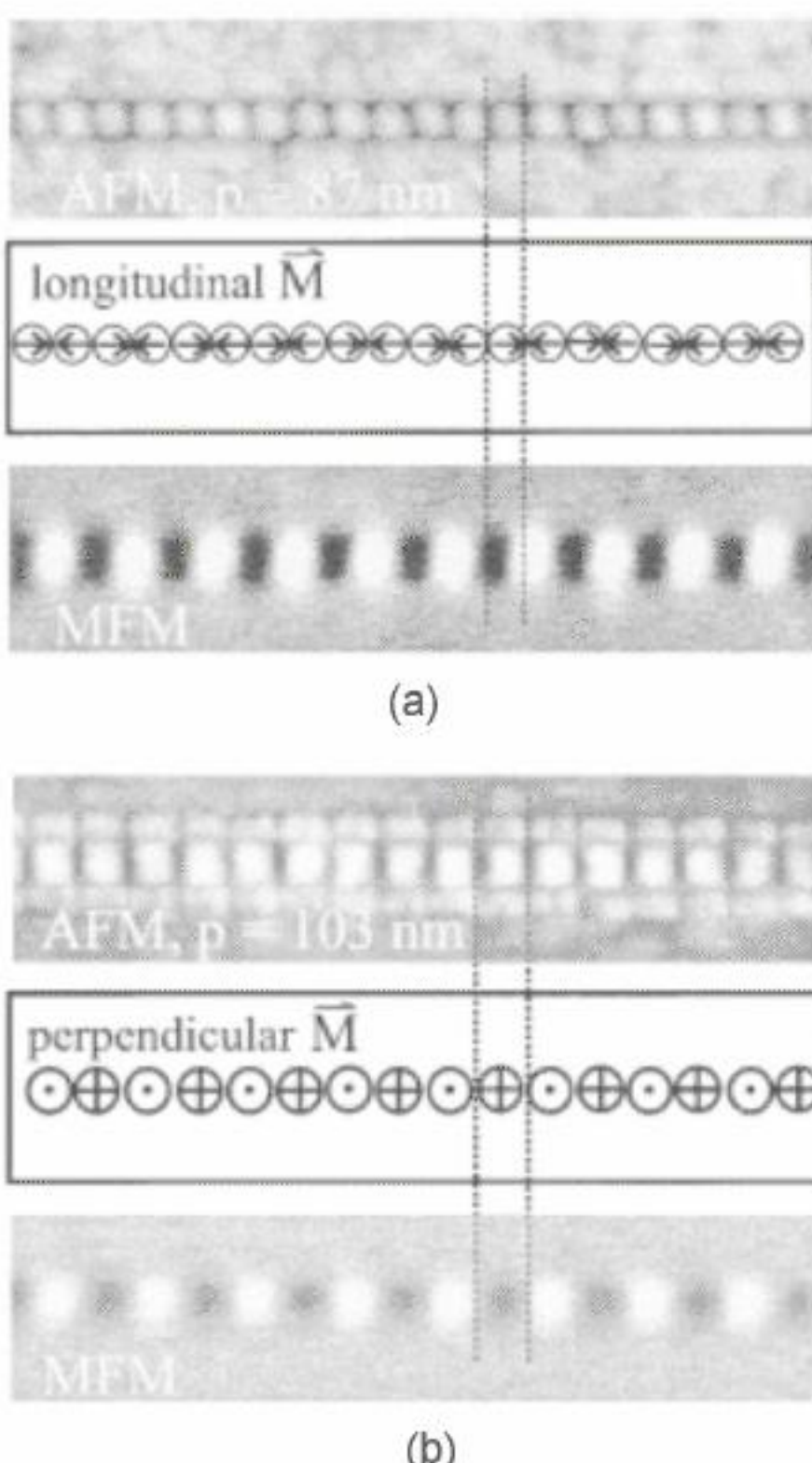


Fig. 8. (a) Longitudinal Co (1010) medium. Top: AFM image of an island row with a period of 87 nm. Bottom: MFM image after in-phase writing. (b) Perpendicular Co₇₀Cr₁₈Pt₁₂ medium. Top: AFM image of an island row with a period of 103 nm. Bottom: MFM image after in-phase writing. For the perpendicular case, the islands in the MFM image are either black or white, depending on their magnetization, while for the longitudinal medium each island appears as a dipole with a black-and-white contrast on either side of the island. (c) Perpendicular CoCrPt medium: GMR readback signals, obtained after applying different phase shifts. (d) Probability to address islands correctly as a function of the phase shift for patterned longitudinal ($p = 60 \text{ nm}$) and patterned perpendicular ($p = 103 \text{ nm}$) media. Corresponding results obtained from a simulation are indicated by dotted and dashed lines. (Reprinted with permission from Ref. 89, © 2003, IEEE)

Patterned media present an intriguing possibility for ultrahigh density data recording further delay of the limitation of superparamagnetic effect. Several fabrication methods of nanoscale patterned particles have been proposed. In addition, recording systems have been investigated on some

key issues, such as read/write methods, synchronization and noise. However, whether patterned media are practically adopted depends on whether this set of complex fabrication, addressing and integration problems can be solved economically. Also, it is crucial to understand the magnetic properties of patterned nanoparticles completely. More explorations and systematic studies are needed and new fabrication methods and recording techniques are expected in the future.

4.3. *Self-assembly of magnetic nanocrystal media*

Patterned media present a potential application for ultrahigh density magnetic storage. One of the challenges for patterned media is whether economical methods exists to prepare nanoscale patterned particles, especially the fabrication of ultrafine, uniformly ordered nanoparticles. To obtain the areal density of 1 Tbit/in², a period with a spacing of 25 nm is required. For 10 Tbit/in², this spacing is reduced to 8 nm. It will be difficult to realize such small spacing periods by the nanofabrication methods. In addition, the high-cost and low throughput limit their application. Therefore, new methods are needed. Chemical synthesis and self-assembly on the substrate of the recording medium may be the most cost-effective method. Compared with lithography, self-assembly of magnetic nanoparticles is inexpensive with a rapid process. Also, by this method, particles with smaller size can be well arrayed. By varying synthesis conditions, different sizes (as small as 2 nm) and shapes of magnetic dots can be prepared. And then, by controlling the conditions of deposition, these monodisperse magnetic nanoparticles can self-organize onto the surface of substrates with two-dimensional (2D) or three-dimensional (3D) superlattice structures. Here, we will focus on synthesis approaches and self-assembly process.

4.3.1. *Chemical synthesis of nanoparticles*

Monodisperse magnetic nanoparticles are of interest as promising candidates to extend the density of data storage media into the range of terabits per square inch.⁹⁰ By careful selection of synthesis conditions, nanocrystals with different shapes and sizes can be fabricated.

So far, many magnetic nanoparticles have been made by the methods above, such as Co,⁹¹ FePt,⁹² FeCo, CoPt, FePd,⁹³ MnFe₂O₄,^{94,95} and Fe₃O₄ (see Fig. 9). Among them, L1₀ FePt is particularly desirable because of its high magnetic anisotropy, small domain wall width (2.8–3.3 nm), small minimal stable grain sizes (2.9–3.5 nm) and chemical stability. In the ordered intermetallic phase, the magnetic anisotropy K_u can reach values as high as 10⁸ erg/cm³, indicating that the magnetic anisotropy energy $K_u V$ (V is the volume of the grain) is much larger than the thermal energy $k_B T$ at ambient temperature. The first successful demonstration of monodisperse FePt nanoparticles was synthesized by decomposition of iron pentacarbonyl [Fe(CO)₅] and reduction of platinum acetylacetone [Pt(acac)₂] in the presence of surfactant molecules, followed by the high temperature annealing process.⁹² However, the chemical composition is difficult to control because of the loss of Fe(CO)₅ during the synthesis.⁹⁶ Without using Fe(CO)₅, monodisperse FePt nanoparticles [shown in Fig. 9(a)] can be made by reducing the reaction of iron(II) and platinum(II) acetylacetones with 1,2-hexadecanediol⁹⁷ as the reducing reagent. The stoichiometry can be adjusted by controlling the molar ratio of Fe(acac)₂ to Pt(acac)₂. Among them, annealed Fe₅₅Pt₄₅ nanoparticles have very high coercivity, $H_c = 9500$ Oe.⁹⁸ The smallest size of FePt nanoparticles can be around 2 nm.⁹⁹ To get larger nanoparticles, seed-mediated growth can be employed, where smaller nanoparticles are used as seeds and more FePt is coated over the seeds.⁹²

Actually, the synthesis of nanoparticles can be controlled by the balance between the nucleation rate and growth rate. If the nucleation period is concurrent with the growth process, the final particle size and shape will be poly-disperse. To realize the separation of the nucleation and growth processes, different methods have been tested. One method is called “injection method”. After injection, fast nucleation occurs, and this is followed by a relatively long growth period. Upon nucleation, the concentration of reactant in solution drops below the critical concentration for nucleation, and further material can only add to the existing nuclei. Growth rate is controlled by the rate of diffusion of reactants to the particles and/or by the reaction rate. Ultimately, the growth will be balanced by the solubility. The size, composition and shape of the particles are controlled by varying the synthesis parameters, such as the molar ratio of stabilizers to metal precursors, the addition sequence of the stabilizers and metal precursors, the heating rate, the heating temperature, the heating duration¹⁰⁰ and the solvent.

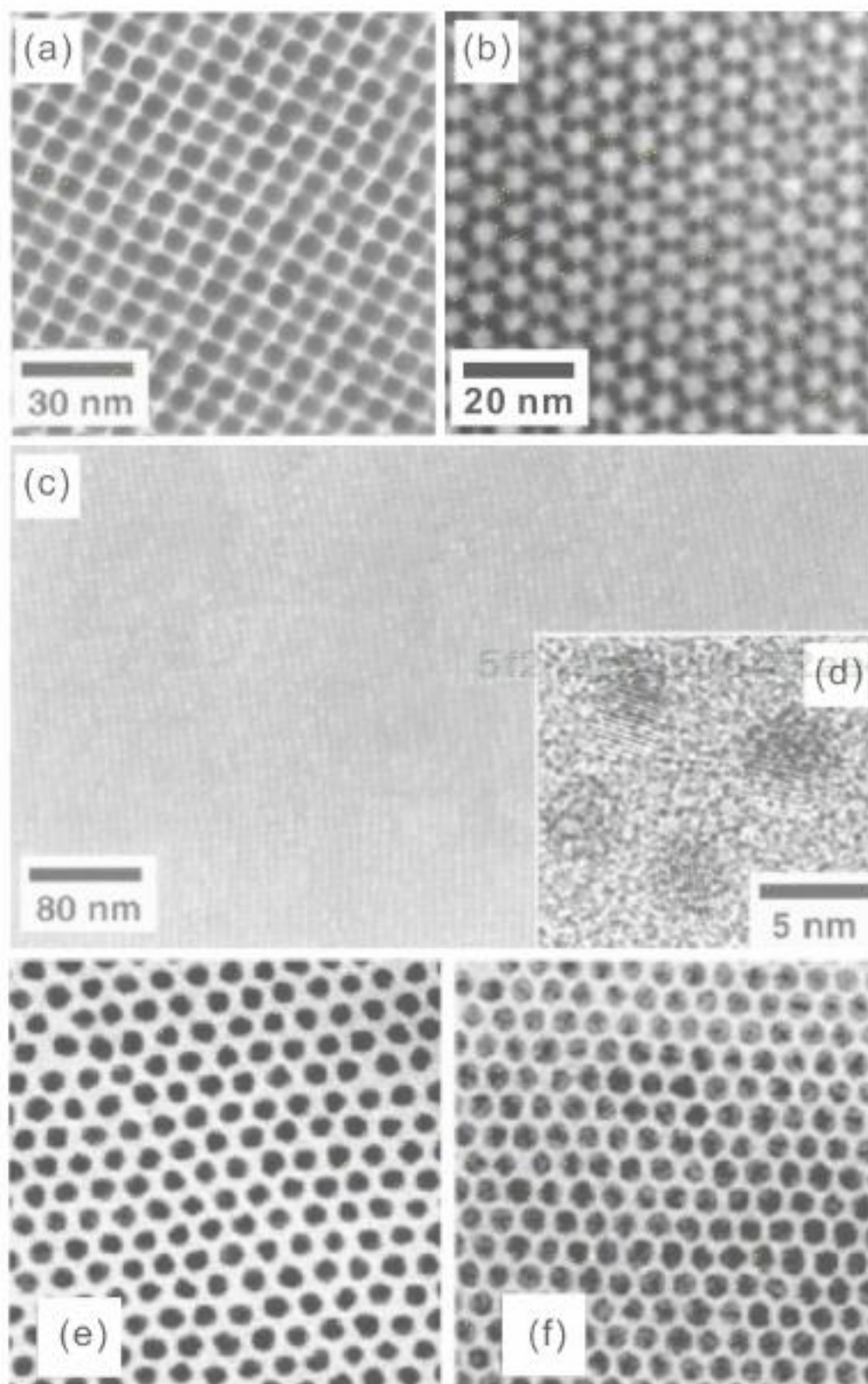


Fig. 9. (a) 3D assembly of a 6 nm $\text{Fe}_{50}\text{Pt}_{50}$ sample after replacing oleic acid/oleyl amine with hexanoic acid/hexylamine.⁹² (b) Monodisperse FePt particles with a 3.01 nm diameter and a standard deviation of 0.29 nm.⁹⁷ (c) HRSEM image of an ~180-nm-thick, 4 nm $\text{Fe}_{52}\text{Pt}_{48}$ nanocrystal assembly annealed at 560°C for 30 min under 1 atm of N_2 gas. (d) High resolution TEM image of 4 nm $\text{Fe}_{52}\text{Pt}_{48}$ nanocrystals annealed at 560°C for 30 min on a SiO-coated copper grid.⁹² (e) Transmission electron microscope image of a Co nanocrystal superlattice before annealing, show in an ~4 nm interparticle distance (the nanocrystal diameter is 10 nm). (f) Co nanocrystal superlattice after annealing (~2 nm interparticle distance).⁹¹ (Reprinted with permission from Refs. 91 and 92, © 2000, American Association for the Advancement of Science)

The first problem encountered in the synthesis process is the aggregation of nanoparticles, caused by van der Waals force of attraction existing in the nanoparticle system. Magnetic interactions between magnetic nanoparticles make this aggregation more serious. The result generates a nondispersed fine powder. In order to avoid this problem, a repulsive or

446bef93ae6067dc
ebrary

stabilizing force is needed. Organic ligands bearing long chain hydrocarbons chains (surfactants) provide a steric repulsion to increase the stability of nanoparticles. Another way is to take advantage of the electrostatic repulsion on the surface of nanoparticles.

Another problem is to prepare nanoparticles with the desired crystallinity. Thermal annealing is necessary to achieve the chemically ordered, high anisotropy ferromagnetic $L1_0$ phase. The high temperature annealing process can lead to nanoparticle agglomeration and sintering. It makes aligning the nanoparticles along the easy axis difficult.^{101,102} In other words, the high temperature annealing process limits the technological applications. One way to decrease the $L1_0$ phase transformation temperature is through addition of Ag to the FePt nanoparticles; yet, 350° C is still necessary for annealing.¹⁰³ Other work included addition of Co to the FePt nanoparticles to improve their physical and magnetic properties.^{103,104} A gas-phase-based process was used to prepare FePt nanoparticles, where the preparation technique allows annealing of the particles in the gas phase prior to their deposition. Higher coercivity was obtained by enhancing the degree of the $L1_0$ order in the gas-phase sintered particles.¹⁰⁵

The solution phase synthesis mentioned above causes the nanoparticles to be encapsulated by organic ligands (such as oleic acid and oleylamine) to prevent aggregation. However, the organic ligand shell can affect both the magnetic properties and the electron configuration of the core. Recently, ligand-free FePt nanoparticles were prepared and their electronic and magnetic properties were characterized.¹⁰⁶ Also, the influence of the surface interaction upon the magnetic properties of $MnFe_2O_4$ nanoparticles with a series of ligands was reported.¹⁰⁷

The biomineral strategy is a potential solution to the synthesis and assembly of crystalline inorganic materials under environmentally benign conditions by controlling the size, composition and phase, in which biological interactions control the nucleation of nanoparticles. So far, using biological templates, narrow size distribution nanoparticles of CoPt¹⁰⁸ and FePt¹⁰⁹ have been prepared. Compared with the approach of chemical synthesis, the development of biological routes for the synthesis of magnetic materials provides a “green” and cost-effective synthetic approach under an ambient environment.

4.3.2. Magnetic nanoparticle self-assembly

Self-assembly is an easy way to produce nanoparticle arrays. By mixing all the chemicals together, nanostructure will be generated automatically by the solvent evaporation. The forces involved in self-assembly include generally weak interactions, such as hydrogen bonding and hydrophobic interaction, steric repulsion, magnetostatic interaction, van der Waals interaction and Coulombic interaction and so on. Among them, which one dominates the behavior of self-assembly depends on the size, size distribution, shape of nanoparticles, and also the properties of solvents. Actually, self-assembled arrays can be fine-tuned. Using the same nanoparticles, different packing styles from hexagonal close packing, square packing, to linear chains were achieved by selecting appropriate conditions.¹¹⁰

The problem here is that the arrays could be easily destroyed since the self-assembly process is driven by weak interactions. This limits the availability and reproducibility of the method. To solve this problem, chemical bonds or other strong interactions must be induced. Template-assisted assembly⁹⁰ was used to assemble the nanoparticles in a controlled manner with robust mechanical properties, in which the substrates are functionalized by special molecules or pretreated to get particular surface structure. For example, organosilane compounds can self-assemble on a hydroxylated surface. Sulfur-containing surfactants are readily absorbed on the surface of gold, silver or copper substrate. These strong molecule–substrate interactions result in “chemical absorption.” Then, by exchanging stabilizers bound to the particles with the molecules that selectively bind to the substrate, nanoparticles can assemble robustly on the surface of the substrate. Alternating adsorption of polyethylenimine (PEI) and FePt nanoparticles on a OH-terminated surface via surface ligand exchange leads to 4 nm FePt nanoparticle assemblies with controlled thickness.^{96,111} As mentioned before, the use of biomolecules as templates for nanoparticle assembly has been proposed recently. For example, a DNA molecule was used as a template for the vectorial growth of a 12-mm-long, 100-nm-wide conductive silver wire,¹¹² and proteins have been reported to direct nanocrystal assembly of semiconductors.¹¹³ The Langmuir–Blodgett method¹¹⁴ was also reported to fabricate FePt nanoparticle media.

4.4. *Organic and molecular magnets*

As mentioned above, all traditional magnetic materials are inorganic materials, such as transition metals and metallic oxides. Their magnetic properties are based on *d/f* orbital electron spins. The introduction of spins into *s/p* orbitals opens up the development of molecule-based magnetic materials, which is important for basic and applied research in science and engineering. Compared with conventional inorganic magnets, molecular magnets present several unique features, such as tunability of properties by means of organic chemistry, easy processability, high mechanical flexibility, low density, low environmental contamination, high compatibility with polymers, high biocompatibility, transparency, semiconducting and/or insulating direct current (d.c.) electrical conductivity, high magnetic susceptibilities, high magnetization and low magnetic anisotropy.¹¹⁵

In the last two decades, much attention has already been directed to the research on molecule-based magnets. Based on the orbital in which spins reside, molecule-based magnets can be grouped into two families.¹¹⁶ One is that the organic fragment is an active component with spin sites contributing to both the high magnetic moment and the spin coupling. The first metal-free organic ferromagnet was discovered 15 years ago. It was a derivative of nitronyl nitroxide, the orthorhombic β -phase crystal of *p*-nitrophenyl nitronyl nitroxide (*p*-NPNN), which became magnetically ordered at 0.65 K.¹¹⁷ Also, thiazyl radicals exhibit magnetic ordering temperatures in excess of 50 K.¹¹⁸ The other group is that the organic fragment only provides a framework to accommodate the spins (which reside solely on metal ions) and facilitates coupling among the spin-bearing metal ions. In the second family, the molecule-based magnets contain metal ions, but are obviously distinct from conventional metal-based magnets, where the organic fragments in the molecules are very important to their magnetic properties. In the following subsection, the structures, the magnetic properties and some mechanisms of molecular magnets will be discussed.

4.4.1. *Magnets with spins only on organic moieties (*p* orbitals)*

4.4.1.1. *Organic radicals*

Being magnetic, at least one unpaired electron (or unpaired spin) exists in the atom or molecule of materials. In organic magnets, organic free

radicals possess an odd number of electrons. The regular array of organic free radicals results in a net magnetization. Since most organic radicals show very low anisotropy, a three-dimensional network of magnetic interactions is required if the material exhibits bulk magnetic order.¹¹⁹ The magnetic properties of organic magnets strongly depend on the exchange interaction of organic free radicals and the solid state structure.^{120–122} However, most organic radicals are extremely unstable and reactive; therefore, they are unable to be isolated in their solid state. To increase the stability of organic radicals, synthetic chemistry is used. One solution is to delocalize the unpaired electron by introducing aromatic rings or adding bulky substituents. The following provides several important organic ferromagnets.

4.4.1.2. Nitronyl-nitroxide-based organic magnets

The first evidence of pure organic long range ferromagnetism was discovered in the β -phase crystal of *para*-nitrophenyl nitronyl nitroxide [*p*-NPNN; the molecular structure is shown in the inset of Fig. 10(a)].¹¹⁶ *p*-NPNN is a very soft ferromagnet [Fig. 10(a)], which saturates in a very small field below the transition temperature ($T_c = 0.65$ K). The magnetic moment in nitronyl nitroxides comes from the unpaired electron that is delocalized over the O–N–C–N–O moiety.

The spin density map [Fig. 10(b)] shows that the positive spin density is delocalized over the nitronyl nitroxide group and also the nitrogen of the nitro group. The spin polarization effects are responsible for the transfer of the spin density to the nitrophenyl group, which means that the intermolecular ferromagnetic interaction passes through both the nitro and the phenyl fragments. Therefore, the substituent group can affect the interaction between neighboring molecules, resulting in modification of crystal structure and the magnetic interaction between unpaired spins.¹²³ Following this discovery, many other nitronyl-nitroxide-based organic ferromagnets have been found. Figure 11 shows some structures of these magnets. Although the chemical modification of the substituent group provides an efficient method for controlling the crystal structure, these nitronyl-nitroxide-based organic radicals still need a very low temperature (below 1 K) to achieve the ferromagnetic order.

5f21ac93d18f02ae446bef93ae6067dc
ebrary

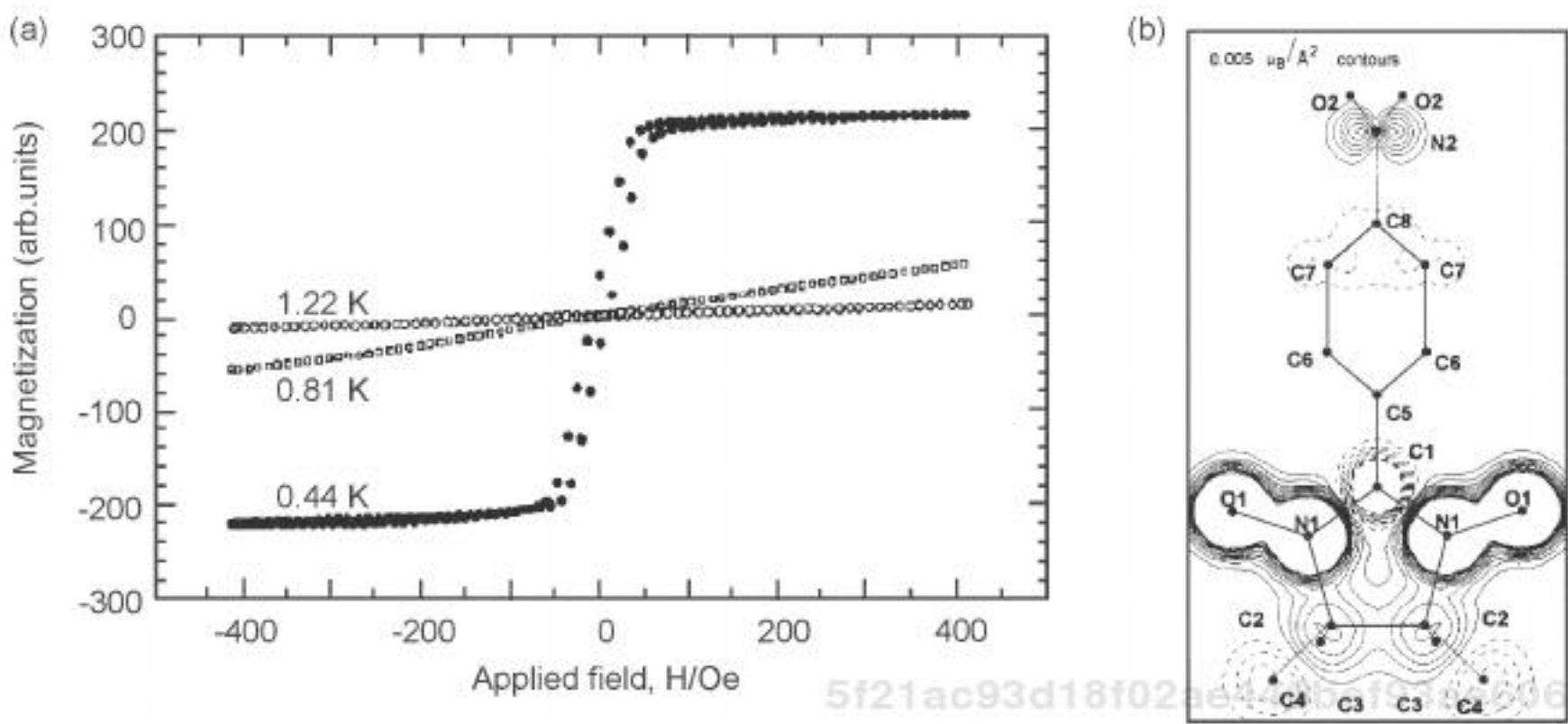


Fig. 10. (a) The magnetization curves of *p*-NPNN, measured at different temperatures ($T_c = 0.65$ K). (Reprinted with permission from Ref. 117, © 1991, Elsevier) The inset shows the molecular structure of *p*-NPNN. (b) The spin density map of *p*-NPNN, obtained from polarized neutron diffraction experiments. (Reprinted with permission from Ref. 123, © 1994, Elsevier)

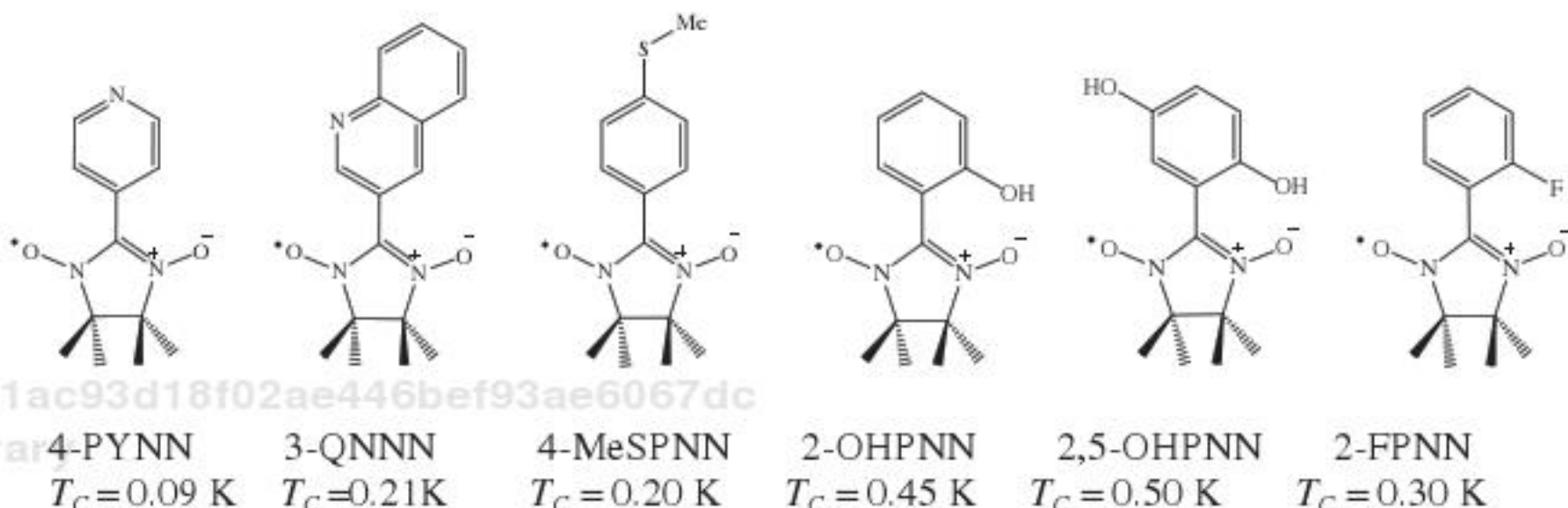


Fig. 11. Some examples of nitronyl-nitroxide-based organic magnets and their transition temperatures.

Other kinds of nitroxide-based radicals exhibiting ferromagnetic interaction have been found, such as the series of 4-(arylmethyleneamino)-2,2,6,6-tetramethylpiperidin-1-oxyls (Ar-CH = N-TEMPO, where Ar = C_6H_5 , 4-Cl-C₆H₄, 4-C₆H₅-C₆H₄, 4-MeS-C₆H₄, 4-C₆H₅O-C₆H₄),^{124,125} nitroxide biradical N,N'-dioxy-1,3,5,7-tetramethyl-2,6-diazaadamantane¹²⁶ and

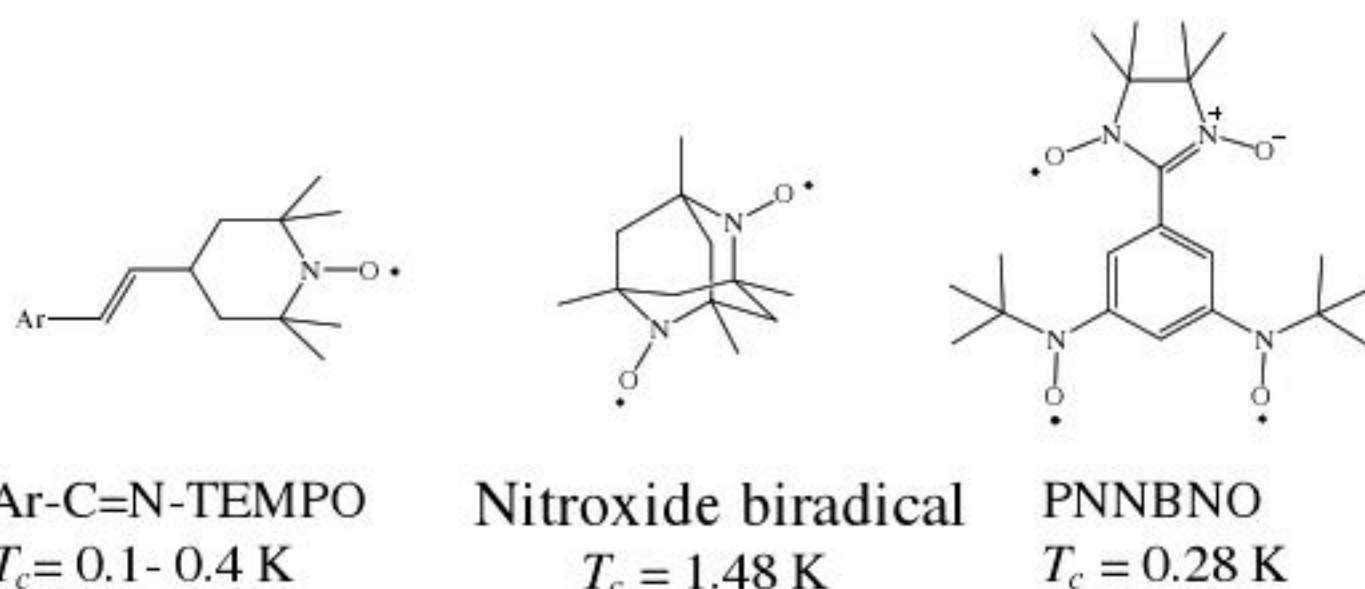


Fig. 12. Some examples of other kinds of nitroxide-based radicals.

asymmetric triradical molecules (2-[3,5-bis(*N*-tert-butylaminoxy)phenyl]-4,4,5,5-tetramethyl-4,5-dihydro-1*H*imidazol-1-oxyl 3-oxide, abbreviated as PNNBNO).¹²⁷ Their molecular structures are shown in Fig. 12. For Ar-C=N-TEMPO, the ferromagnetism transition temperature is also very low, which is believed to be due to the weak dipolar coupling between ferromagnetic layers. The diradical exhibits the highest T_c among them, which order ferromagnetically at 1.48 K.¹²⁶ PNNBNO includes an $S = 1$ and an $S = 1/2$ unit within a single molecule and the two units are connected by intra- and intermolecular antiferromagnetic interactions. The 3D phase transition occurs at 0.28 K.¹²⁷

Besides nitroxide-based radicals, verdazyl radicals and sulfur-based radicals also show ferromagnetic intermolecular interactions. For example, ferromagnetism has been observed in 3-(4-chlorophenyl)-1,5-diphenyl-6-oxoverdazyl (*p*-CdpOV; the molecular structure is shown in Fig. 13) with $T_c = 0.21\text{ K}$.¹²⁸ The β -phase of the dithiadiazolyl radical (*p*-NCC₆F₄CNSN, the molecular structure is shown in Fig. 13) exhibits noncollinear antiferromagnetism at 35.5 K.¹²⁹ One interesting example is 1,3,5-trithia-2,4,6-triazapentalenyl (TTA, the molecular structure is shown in Fig. 13). It has a large first order magnetic phase transition over the temperature range of 230–305 K from the high temperature paramagnetic phase to the low temperature diamagnetic phase. The magnetic bistability originates from different molecular arrangement and this property is very helpful in data storage.¹³⁰

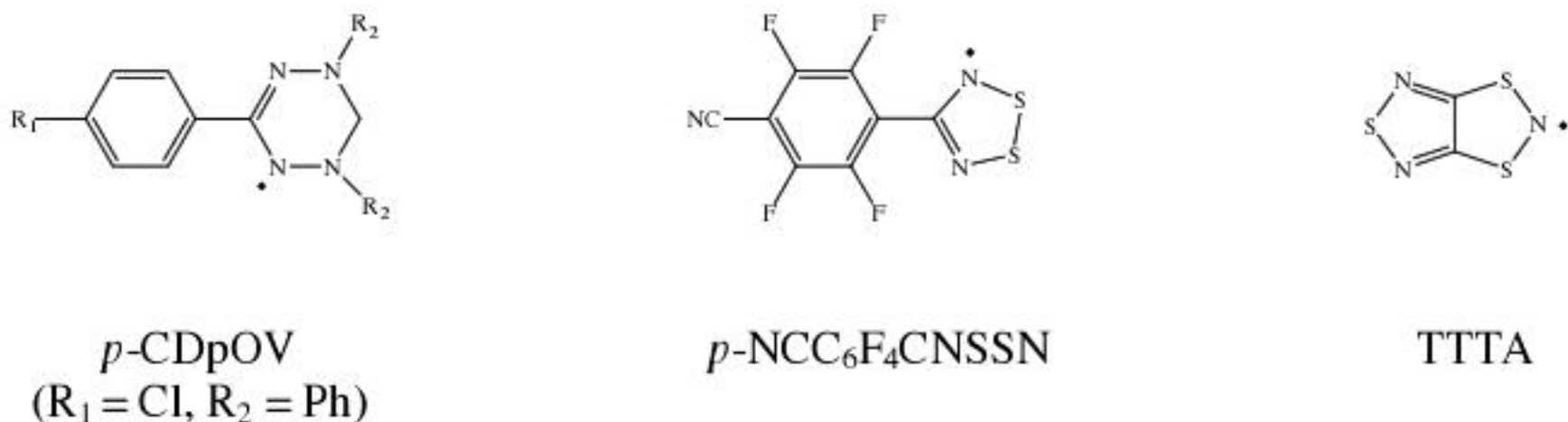


Fig. 13. Some examples of verdazyl radicals and sulfur-based radicals.

4.4.1.3. Fullerenes

Tetrakis(dimethylamino)ethylene-fullerene(60) (TDAE-C₆₀) is a donor-acceptor type magnetic material. The α -phase crystal shows a ferromagnetic state with fully saturated $s = 1/2$ molecular spins at a relatively high Curie temperature, $T_C = 16$ K.¹³¹ The later research results showed that the sample preparation was crucial for the magnetic properties.¹³² Fresh single crystals of TDAE-C₆₀ grown below 10°C (the α -phase), show no ferromagnetic behavior when cooled down to 2 K [Figs. 14(a) and 14(b)].¹³² The different properties between these two crystal forms come from the different orientation of the C₆₀ molecules in the two-phases [Fig. 14(c)]. By annealing at high temperature, the α -phase can turn into the ferromagnetic α -phase. After this discovery, much attention has been given to fullerene and fullerides.

The fullerene-based materials showed a slight increased transition temperature, such as 3-aminophenyl-methano-fullerene(60)-cobaltocene with $T_C = 19$ K¹³³ But the transition temperatures were still very low until the advent of the rhombohedral C₆₀ polymer (Rh-C₆₀).¹³⁴ The magnetic carbon of Rh-C₆₀ is prepared at high temperature and pressure; the magnetic phase appears when fullerene cages are about to break down and form graphitized fullerene. The formation of the graphitized fullerene is a 2D rhombohedral polymer phase, composed of layers of covalently bonded C₆₀ molecules. The saturation magnetization and Curie temperature are determined by preparation conditions. The highest T_C is 820 K.¹³⁵ Ferromagnetic ordering in a hydrofullerite C₆₀H₂₄ with $T_C = 300$ K has also been found.¹³⁶ The total concentration of magnetic impurities

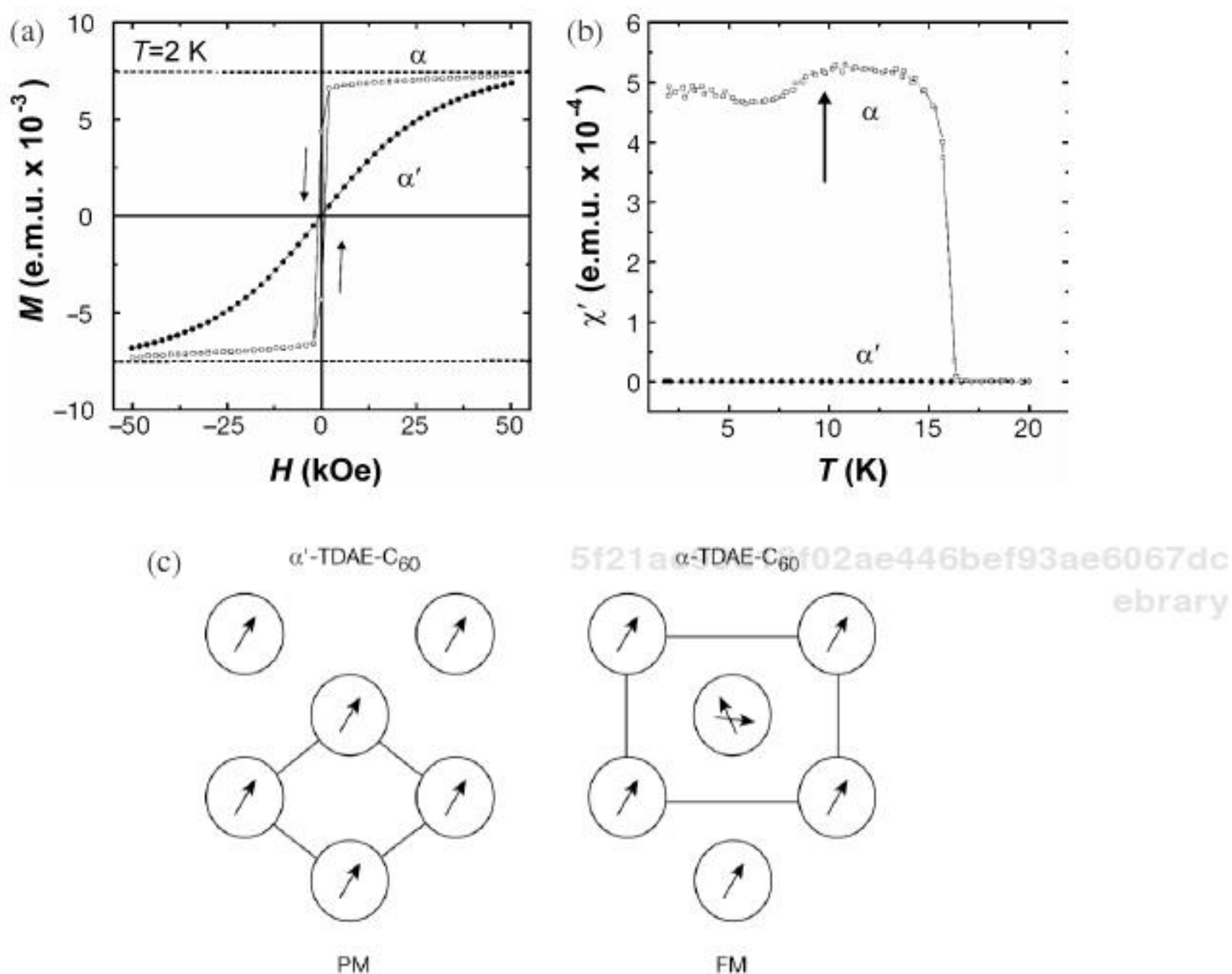


Fig. 14. (a) Magnetization curves of the PM and FM samples of TDAE- C_{60} (dots and squares, respectively). (b) The a.c. susceptibility χ of the PM and FM samples. The arrow shows a dip in the susceptibility due to the onset of glasslike behavior, as suggested by the model. (c) Schematic diagram of the C_{60} molecular orientations in the $a-b$ plane for the PM (left) and FM structures (right). (Reprinted with permission from Ref. 143, © 1987, 5f21ac93d18f02ae446bef93ae6067dc American Physical Society) ebrary

reported in those studies appears to be too low to give rise to the observed magnetization.¹³⁴ However, the new experimental and theoretical results concluded that the rhombohedral distortion of C_{60} itself cannot induce magnetic ordering in the molecular carbon,¹³⁷ and suggested that hydrogen may play an important role in the magnetic ordering found in fullerenes.¹³⁸ To fully understand the mechanism, further experimental and theoretical work is required. Although the mechanism is still unclear and the magnetism is very weak, the discovery of Rh- C_{60} still gives a new perspective in the investigation of organic magnets with highly tunable properties for use in magnetic devices.

4.4.2. Magnets with spins on both metal ions and organic moieties (p and d/f orbitals)

One route to increase the transition temperature is to prepare hybrid materials, in which organic groups are bonded with transition metals and they both have unpaired spins. This family of magnets includes charge transfer (CT) salts and metal–radical complexes.

4.4.2.1. Charge transfer salts

The most famous type of CT salt ferromagnet is the metallocene-based molecular magnet $[MCp^*_2][\text{organic acceptor}]$ ($M = \text{metal}$, Cp^* = C_5Me_5 /pentamethylcyclo-pentadienide). The metallocenes mainly include FeCp^*_2 , MnCp^*_2 and CrCp^*_2 .

The first MCp^*_2 CT salt discovered to have a ferromagnetic ground state was $[\text{FeCp}^*_2][\text{TCNE}]$ with $T_C = 4.8 \text{ K}$ [$\text{TCNE} = \text{tetracyanoethylene}$; the molecular structure is shown in Fig. 15(a)].¹³⁹ The magnetization shows hysteresis as a function of varying applied magnetic field, with a coercive force reaching as high as 1000 G at 2 K [Fig. 15(b)]. Further studies, replacing Fe(III) with Mn(III)¹⁴⁰ and Cr(III),¹⁴¹ yielded new ferromagnets, each having unpaired electrons ($[\text{FeCp}^*_2]^+$, $S = 1/2$; $[\text{MnCp}^*_2]^+$, $S = 1$; $[\text{CrCp}^*_2]^+$, $S = 3/2$). The transition temperatures decrease following the order of $\text{Mn} > \text{Fe} > \text{Cr}$. The organic acceptor, TCNE, is a planar molecule with strong electron withdrawing groups ($-\text{C}\equiv\text{N}$), which helps to stabilize the radical anion formed through accepting an electron. One interesting discovery was $\text{V}(\text{TCNE})_x \cdot y\text{CH}_2\text{Cl}_2$, obtained from the reaction of bisbenzene vanadium with TCNE in dichloromethane, which exhibits a high magnetic ordering temperature, $T_C = 400 \text{ K}$.¹⁴²

The CT salts of MCp^*_2 ($M = \text{Fe, Mn, Cr, V, ...}$) and organic acceptors can be synthesized by a simple process, i.e. mixing the donor and acceptor in a polar solvent, and the CT salt can be precipitated by adding a nonpolar solvent (see Fig. 16). The choice of solvent for the synthesis is very important. It is believed that the solvent may affect the donor–acceptor stacking structure.¹³⁸ Considering the stability, synthesis of some CT salts requires an inert atmosphere and a special low temperature. The electron transfers from a metallocene to an organic acceptor and a CT salt forms

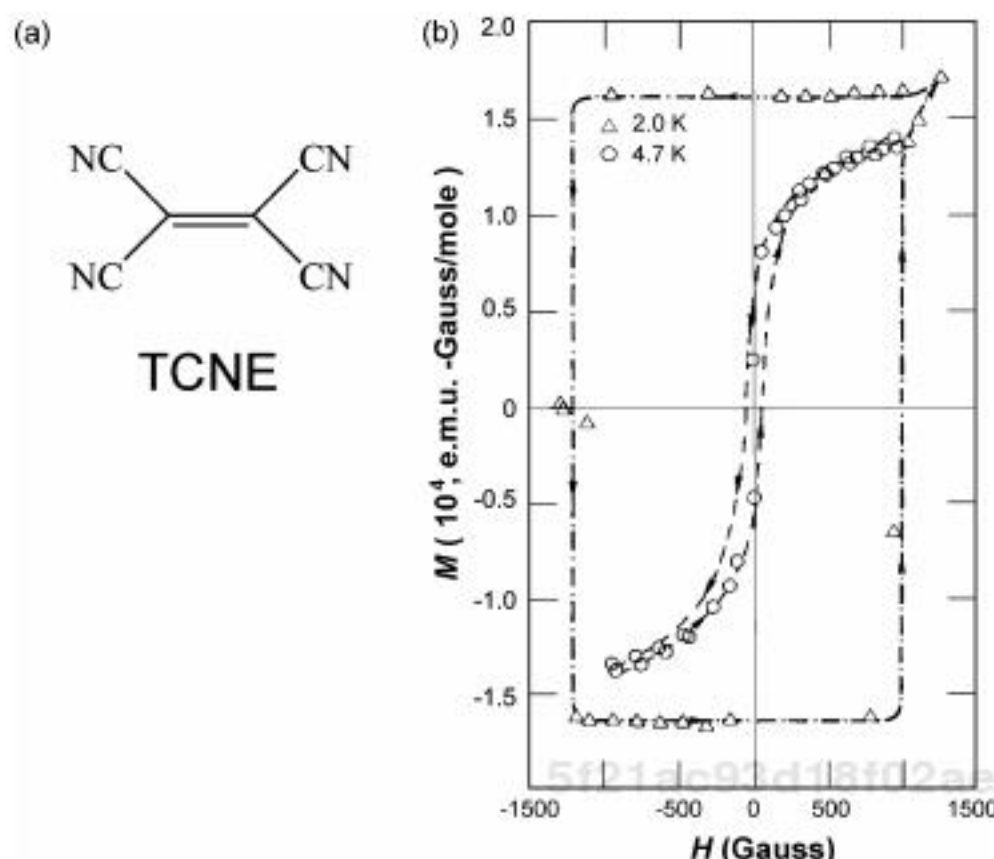


Fig. 15. (a) Molecular structure of TCNE and (b) magnetization data for $[\text{FeCp}^*]^2\text{TCNE}$ at 2.0 K and 4.7 K. (Figure (b) is reprinted with permission from Ref. 143, © 1987, American Physical Society).

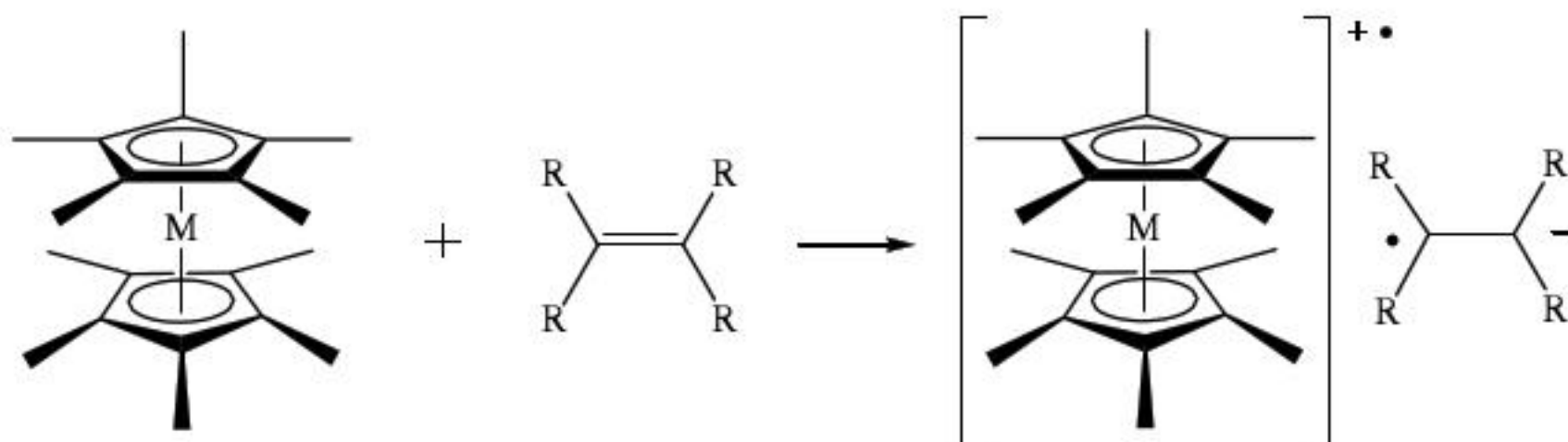


Fig. 16. Formation of CT salt by electron transfer from a metallocene donor to an organic acceptor ($\text{M} = \text{Fe}, \text{Mn}, \text{Cr}, \text{V}, \dots$; R = electron withdrawing group, such as $-\text{CN}$).

with unpaired electrons on both the metallocenium ion and the organic radical anion.

Since TCNE was used for the synthesis of CT salts, efforts on the CT salts also resulted in the discovery of other organic acceptors with similar structure. 7,7,8,8-tetracyano-p-quinodimethane (TCNQ) is a typical organic electron acceptor (the molecular structure is shown in Fig. 17). The difference from TCNE is spin in TCNQ was delocalized over more atoms, resulting in lower spin density and weaker spin coupling. Actually,



Fig. 17. Some examples of organic acceptors and donors.

the transition temperatures of TCNQ counterparts are lower than that of TCNE salts. R₁,R₂-DCNQI (DCNQI = N,N'-dicayanoquinodimine) is another example of an organic acceptor (the molecular structure is shown in Fig. 17). Cu-(Me₂DCNQI)₂ was noted for high conductivity.^{144,145} The strong interlattice interaction between the *d* electrons of Cu and the π electrons in *p* orbitals from DCNQI delocalizes the electron energy. By changing the temperature, pressure or selective deuteration, conductivity and susceptibility can be obtained from metal to insulator, from antiferromagnetic order to ferromagnetic state.¹⁴⁴ Besides organic acceptors, CT salts can also be formed by combining a metal complex with an organic donor, such as tetrathiafulvalene (TTF) as an electron donor. TTF can be combined with metal-anion complexes to form CT salts, such as TTF₁₄(MCl₄)₄ (M = Mn, Co)¹⁴⁶ and TTF₇(FeCl₄)₂.¹⁴⁷

4.4.2.2. Metal–radical complexes

Metal–radical complexes assemble the organic radical centers by means of complexation with paramagnetic transition metal ions. One example is Mn^{II}(hfac)₂-nitroxide system (Mn^{II}(hfac)₂ = bis(hexafluoroacetylacetonato)manganese(II)), where a linear trifunctional nitroxide results in the formation of 2D/3D structure ferro/ferrimagnets.

When [Mn^{II}(hfac)₂] was treated with highly symmetric trinitroxide radical 1 [the molecular structure is shown in Fig. 18], the expected 3:2 complex with a 2D network structure was obtained. The complex became a magnet with $T_C = 3.4$ K, which was ascribed to the weak intramolecular exchange coupling ($J_{\text{intra}} = 6.8$ K) of 1.¹⁴⁹ When radicals with strong intramolecular exchange coupling were used, such as 2 [Fig. 18(a)] with

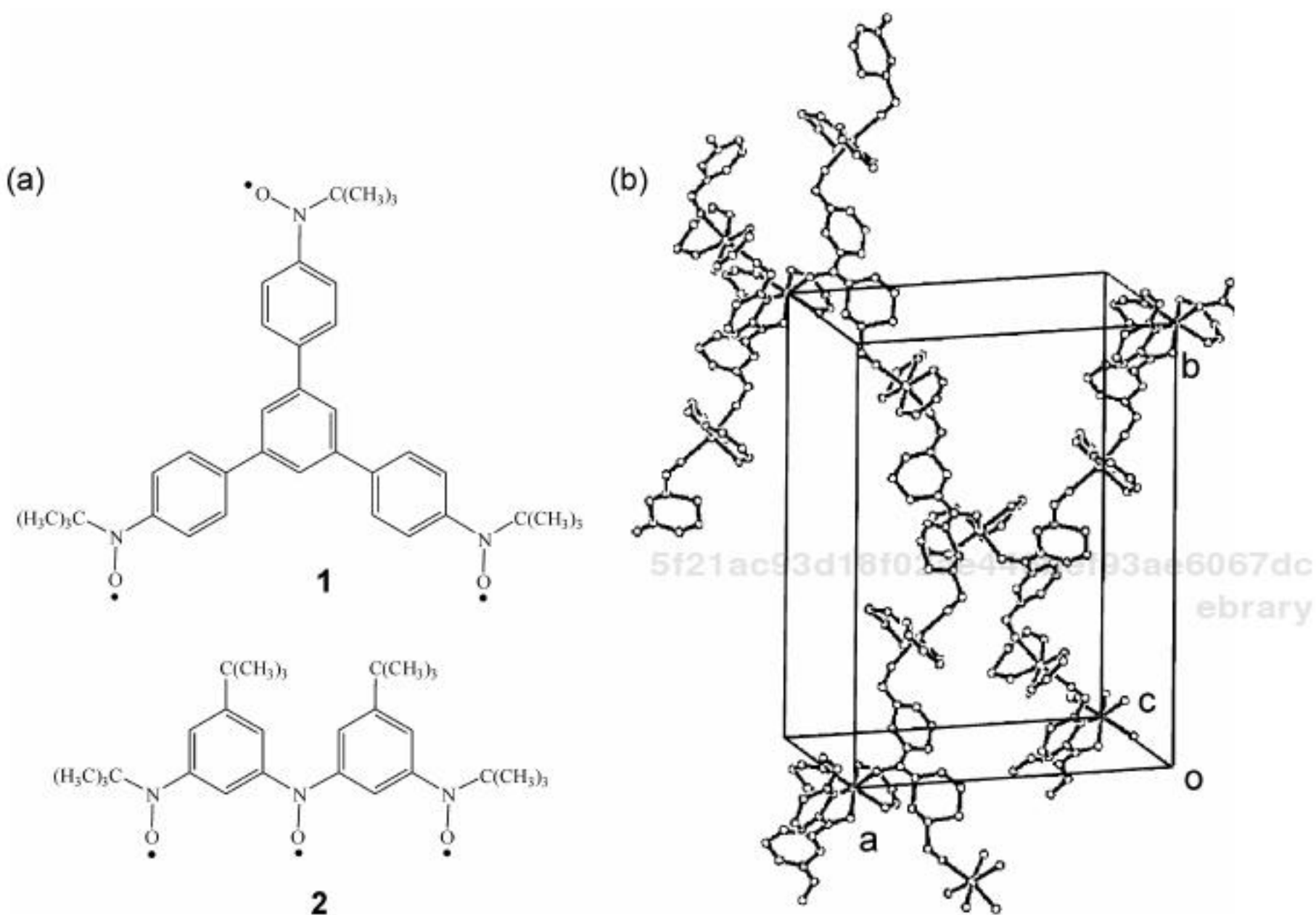


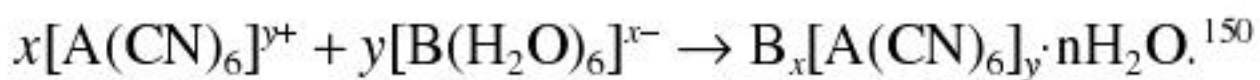
Fig. 18. (a) Molecular structure of radicals 1 and 2; (b) packing structure of the 3D polymer complex $[\text{Mn}^{\text{II}}(\text{hfac})_2]_3 \cdot 2_2$. (Reprinted with permission from Ref. 148, © 1996, American Chemical Society)

$J_{\text{intra}} = 240$ K, a 3D polymeric network was formed and magnetization was obtained at $T_C = 46$ K,¹⁴⁸ which arose from ferro- and anti-ferromagnetic coupling (in different directions) [3D packing structure is shown in Fig. 18(b)]. In these complexes, the $2p$ spins of the organic ligands and the $3d$ spins of Mn(II) in ferrimagnetic coupling are the origin for the observed magnetization.

4.4.2.3. Magnets with spins on organic moieties and metal ions providing exchange pathways

Prussian blue, $\text{Fe}^{\text{III}}_4[\text{Fe}^{\text{II}}(\text{CN})_6]_3 \cdot n\text{H}_2\text{O}$, and its analogues, $\text{A}_x[\text{B}(\text{CN})_6]_y \cdot n\text{H}_2\text{O}$ ($\text{A} = \text{Cu, Ni, Co, Fe, Mn}; \text{B} = \text{Cr, Mn, Fe, Co}$), have attracted attention due to their color, as well as their special properties, such as photo-induced magnetic switching and tunable and high Curie temperatures.

These compounds are generally synthesized via Lewis acid–base reactions in water:



Most of these hexacyanometalate-based products adopt a simple face-centered cubic lattice, in which adjacent metals A and B are connected through cyanide bridges forming the linear B–CN–A alignment. The Kahn model applied to such a system realizes that only a t_{2g} (π symmetry) orbital exists on the B site, whereas on the A site both t_{2g} and e_g are present [shown in Fig. 19(a)]. Two kinds of orbital pathways are possible: antiferromagnetic ones, t_{2g} - t_{2g} [Fig. 19(b)], and ferromagnetic ones, t_{2g} - e_g [Fig. 19(c)].¹⁵¹ The coupling constant, J , is the magnitude of the exchange interaction, which can be tuned by tuning the electronic configuration of A. Since $T_C \propto z|J|$,^{126,152} the Curie temperature can be adjusted. For example, crystalline $\text{V}^{\text{II}}[\text{Cr}^{\text{III}}(\text{CN})_6]_{0.86} \cdot 2.8\text{H}_2\text{O}$ has a T_C value of 315 K, but the T_C of $\text{K}^{\text{I}}\text{V}^{\text{II}}[\text{Cr}^{\text{III}}(\text{CN})_6]$ is 376 K. Table 3 lists some representatives of Prussian blue analogues, T_C and their magnetic behavior.

4.5. Single molecule magnets

The above molecule-based magnetic compounds normally contain few transition metal ions, such as Mn, Fe, V, Ni, Cr and Co. Another type of molecule-based magnetic compounds is several polynuclear cage metal complexes with a large spin S , resulting from the intramolecular exchange between the transition metal ions in the cluster. This opened up a new area of high spin metal clusters, termed “single molecule magnets” (SMMs).

The first identified SMM was a manganese oxide cluster with acetate ligands, $\text{Mn}_{12}\text{O}_{12}(\text{O}_2\text{CCH}_3)_{16}(\text{H}_2\text{O})_4$, which was synthesized by the reaction of $\text{Mn}(\text{O}_2\text{CCH}_3)_2$ with KMnO_4 in CH_3COOH and water solution. This cluster has 4 Mn(IV), 8 Mn(III), 20 unpaired electrons, and crystallizes with tetragonal (axial) symmetry¹⁶² [the structures are shown in Fig. 20(a)]. The studies of the magnetic properties showed the low temperature magnetic susceptibility¹⁶³ and also magnetic hysteresis.¹⁶⁴ The large ground state spin is caused by the exchange interactions between the $S = 2$ spins of the Mn(II) ions and the $S = 3/2$ spins of the Mn(IV) ions. Here the four central Mn(IV)

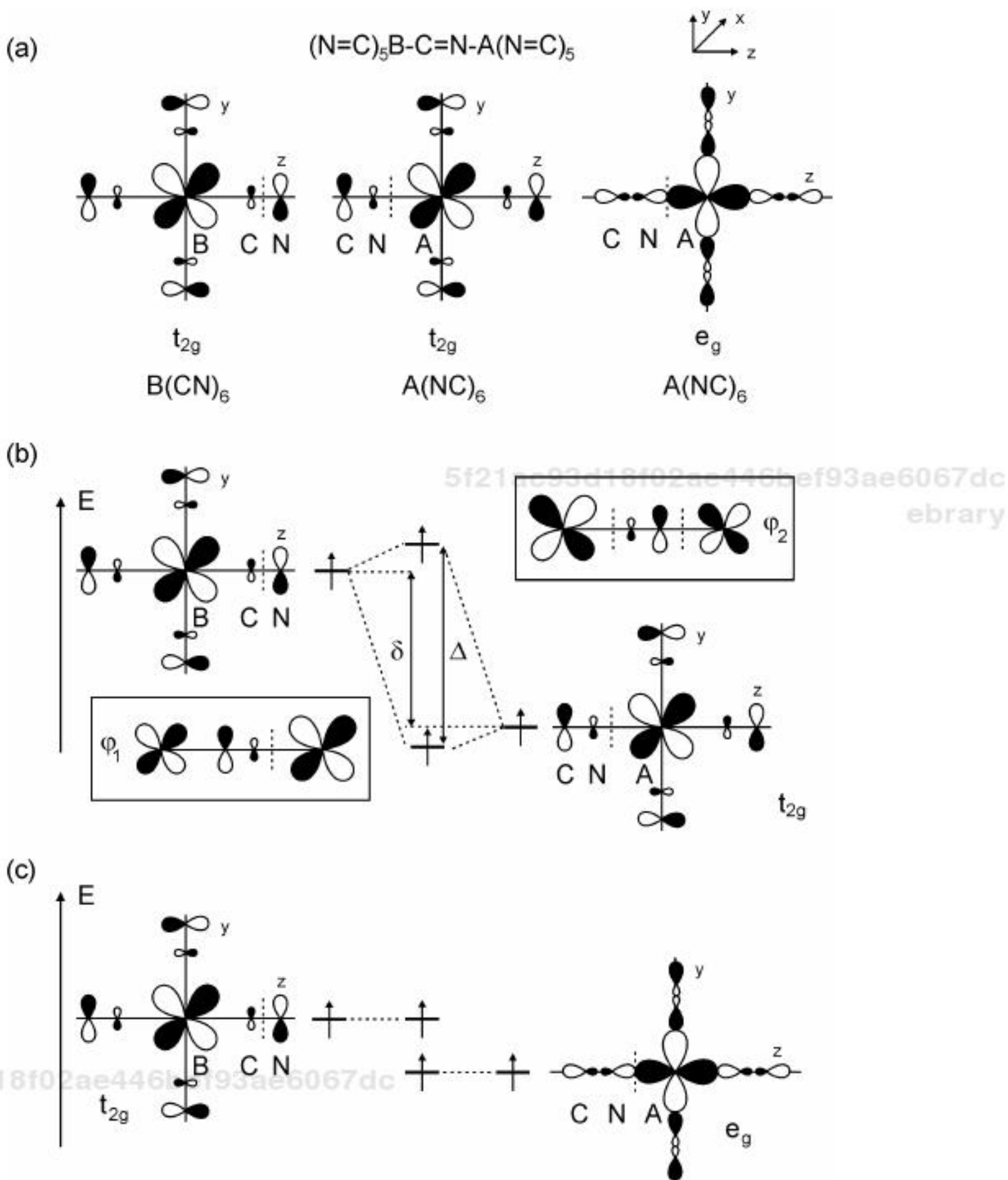


Fig. 19. (a) Magnetic orbitals: (A) t_{2g} in $B(CN)_6$; (B) t_{2g} in $A(NC)_6$; (C) e_g in $A(NC)_6$. (b) Interaction between overlapping t_{2g} magnetic orbitals in $(NC)_5B(CN)A(NC)_5$. (c) Orthogonal t_{2g} and e_g magnetic orbitals in $(NC)_5B(CN)A(NC)_5$. (Reprinted with permission from Ref. 151, © 2001, Elsevier)

centers spin in the opposite direction to those eight outer Mn(III) centers [Fig. 20(b)]. Then the total S is equal to $|(4 \times 2/3) + [8 \times (-2)]| = 10$.^{165,166}

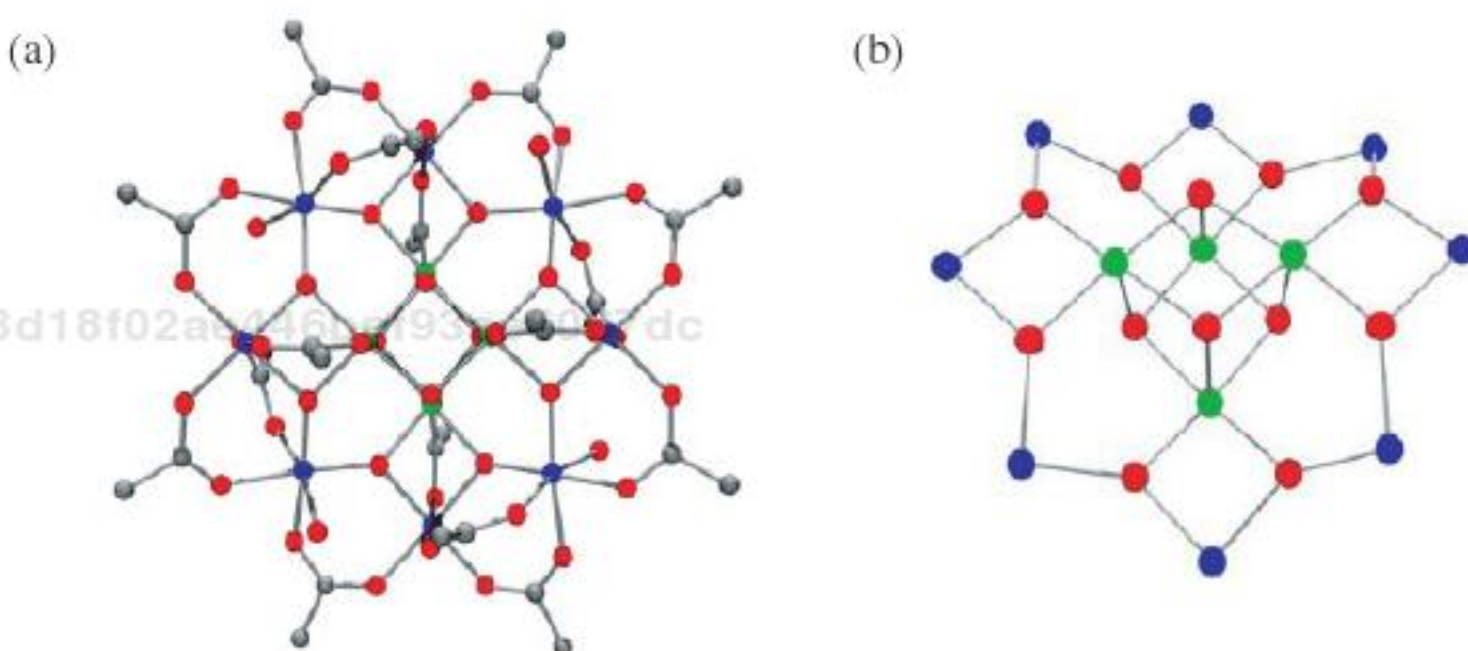
The eight Mn(III) ions on the outer periphery undergo a Jahn–Teller (JT) elongation in the z -direction, which leads to the magnetic moment of an individual Mn_{12} molecule preferentially lying in the z -direction, or the

Table 3. Some representatives of Prussian blue analogues.

Composition	T_c/K	Ordering	Reference
$\text{Fe}^{\text{III}}_4[\text{Fe}^{\text{II}}(\text{CN})_6]_3 \cdot n\text{H}_2\text{O}$, Prussian blue	5.6	FO	153
$\text{Cs}^{\text{I}}\text{Ni}^{\text{II}}[\text{Cr}^{\text{III}}(\text{CN})_6] \cdot 2\text{H}_2\text{O}$	90	FO	154
$\text{CsMn}^{\text{II}}[\text{Cr}^{\text{III}}(\text{CN})_6] \cdot \text{H}_2\text{O}$	90	FI	155
$\text{Cr}^{\text{III}}[\text{Cr}^{\text{III}}(\text{CN})_6]_{0.93}[\text{Cr}^{\text{II}}(\text{CN})_6]_{0.05}$	260	FI	156
$\text{V}^{\text{II}}_{0.45}\text{V}^{\text{III}}_{0.53}[\text{V}^{\text{IV}}\text{O}]_{0.02}[\text{Cr}^{\text{III}}(\text{CN})_6]_{0.69}$ $(\text{SO}_4)_{0.23} \cdot 3.0\text{H}_2\text{O} \cdot 0.02\text{K}_2\text{SO}_4$	310	FI	157
$\text{Cs}_{0.82}\text{V}^{\text{II}}_{0.66}[\text{V}^{\text{IV}}\text{O}]_{0.34}[\text{Cr}^{\text{III}}(\text{CN})_6]_{0.92}$ $[\text{SO}_4]_{0.203} \cdot 3.6\text{H}_2\text{O}$	315	FI	157
$\text{V}^{\text{II}}[\text{Cr}^{\text{III}}(\text{CN})_6]_{0.86} \cdot 2.8\text{H}_2\text{O}$	315	FI	158
$\text{K}^{\text{I}}_{0.058}\text{V}^{\text{II}/\text{III}}[\text{Cr}^{\text{III}}(\text{CN})_6]_{0.79}$ $(\text{SO}_4)_{0.058} \cdot 0.93\text{H}_2\text{O}$	372	FI	159
$\text{K}^{\text{I}}\text{V}^{\text{II}}[\text{Cr}^{\text{III}}(\text{CN})_6]$	376	FI	160

FO = Ferromagnet

FI = Ferrimagnet

Fig. 20. Structure of (a) the $[\text{Mn}_{12}\text{O}_{12}(\text{O}_2\text{CCH}_3)_{16}(\text{H}_2\text{O})_4]$ complex and (b) the $[\text{Mn}_{12}\text{O}_{12}]^{16+}$ core — Mn(IV), green; Mn(III), blue; O, red; C, gray. (Reprinted with permission from Ref. 161, © 2005, University of Florida)

easy axis. The magnetic anisotropy of this easy axis type is negative, $D = -0.5 \text{ cm}^{-1}$. In zero-field splitting, the $S = 10$ ground state spin is divided into 21 (i.e. $2S + 1$) sublevels, the energy of each sublevel $E = m_s^2 D$ (m_s , spin projection quantum number — $S \leq m_s \leq S$). So when $m_s = \pm 10$ (spin

orientations: spin-up and spin-down), the energy of sublevels is lowest; and when $m_s = 0$, the energy is highest. As a consequence, there is a spin reversal energy barrier, $U = S^2|D|$ (for the Mn_{12} cluster, $U = 100|D| = 50\text{ cm}^{-1}$), between the two spin orientations of the magnetic moment.

The relationship between the relaxation time τ and U can be given by the Arrhenius equation: $\tau = \tau_0 \exp(U_{\text{eff}}/k_B T)$. When temperature T is greater than U/k_B , the magnetization can fluctuate. On the contrary, the magnetization is stable. In the case of $T \ll U/k_B$, the magnetization becomes “fixed” because of the exponential in the equation. This is the reason that SMMs exhibit slow (or temperature-independent) magnetization relaxation at low temperature. The a.c. magnetic susceptibility measurements indicate that the slow magnetization relaxation present by an SMM is intrinsic to the molecule itself and not to long range interactions.^{167,168}

The slow relaxation of the magnetization in SMMs also leads to magnetic hysteresis. The magnetic hysteresis loops get narrow when the temperature increases (see Fig. 21),¹⁶⁵ so variation of temperature can strongly affect the coercivity of the sample. The quantum tunneling of magnetization (QTM) through the energy barrier U results in a loss of spin polarization in the molecule. In Fig. 21, this effect is shown as the steps on loops.

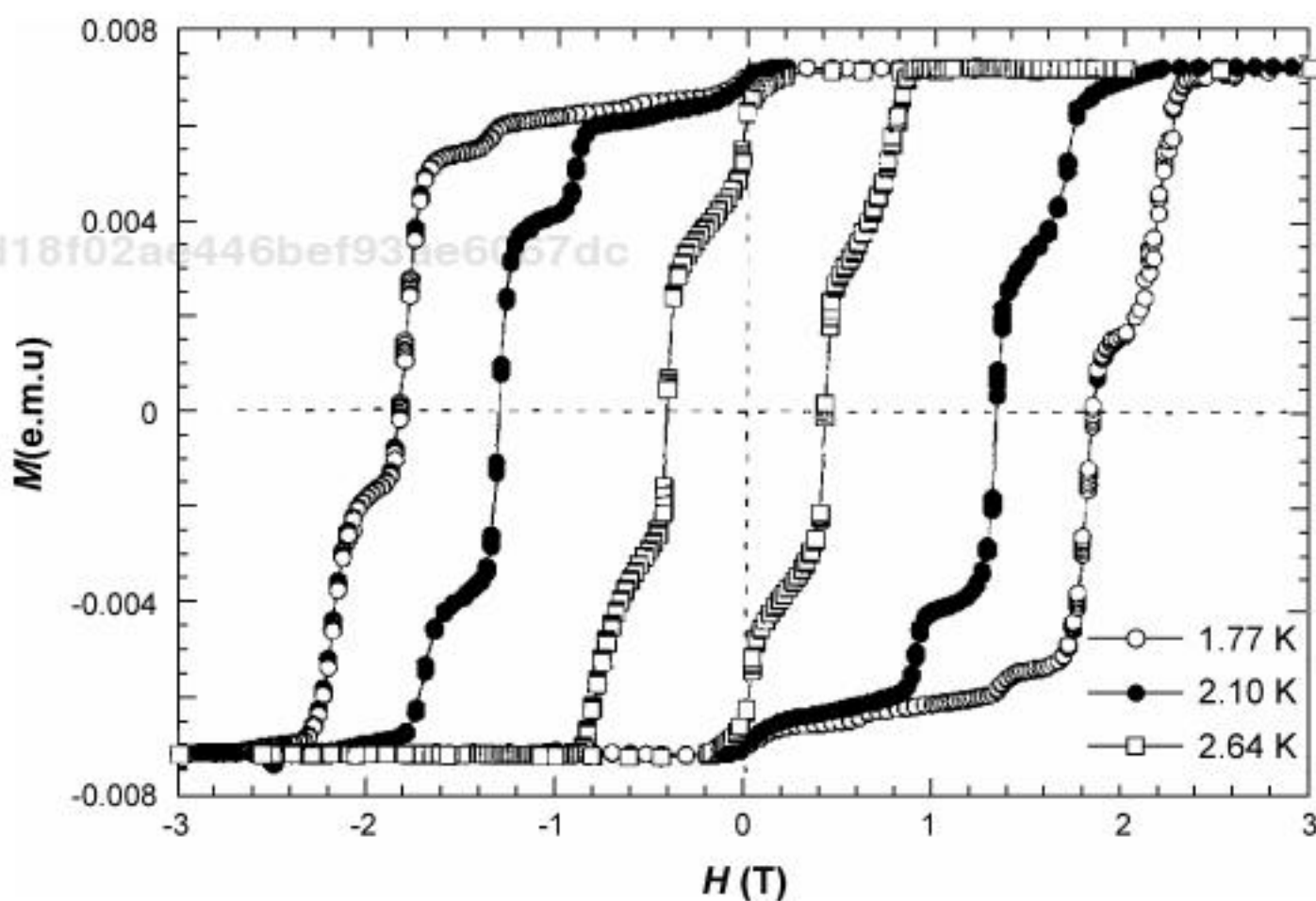


Fig. 21. Magnetic hysteresis loop measured on the Mn_{12} cluster at different temperatures: 1.77 K, 2.10 K and 2.64 K. (Reprinted with permission from Ref. 165, © 1996, Nature Publishing Group)

The discovery of the SMM of Mn_{12} clusters has created great interest in this field. Much work has been done to explore other molecules exhibiting similar magnetic properties. Among them, the Fe_8 cluster is another important SMM.¹⁶⁹ The formula of the Fe_8 cluster is $[Fe^{III}_8O_2(OH)_{12}(tacn)_6]^{8+}$ ($tacn = 1,4,7$ -triazacyclononane), with a ground spin state $S = 10$ (two iron atoms' moments align opposite to the field and the other six parallel to the field, i.e. $S = 6 \times 5/2 - 2 \times 5/2 = 10$), axial anisotropy $D = -0.19\text{ cm}^{-1}$ and the effective energy barrier $U_{\text{eff}} = 15\text{ cm}^{-1}$. The weaker anisotropy makes low temperature relaxation measurements experimentally feasible. Compared with Mn_{12} clusters, ground state quantum tunneling (i.e. tunneling between the lowest energy m_s ($m_s = \pm 10$) levels) was first observed in Fe_8 clusters,¹⁶⁹ but the QTM in Mn_{12} clusters occurs between higher energy sublevels ($-10 < m_s < 10$).¹⁷⁰ The latter phenomenon is also called thermally-assisted tunneling. During this tunneling process, molecules on the ground state ($m_s = \pm 10$, either one) sublevel are first thermally activated to higher sublevels, through which tunneling of the magnetization occurs. The difference between these two magnetic relaxations can be attributed to the greater transverse anisotropy, which leads to a high degree of mixing between the $m_s = \pm 10$ levels and facilitates tunneling.

So far in the SMM family, the most salient structure is perhaps the Mn_{84} cluster,¹⁷¹ which is the largest SMM (with an outside diameter of 4.2 nm and a thickness of 1.2 nm), synthesized by the reaction of Mn_{12} acetate clusters with a premanganate salt. The cluster crystallizes in hexagonal arrays, like a holiday wreath. The multiple layers align to form nanotubes that offer various possibilities in future applications. Besides these oxide bridging compounds, other clusters (such as cyanide bridging groups) were also made. Mn_4Re_4 ¹⁷² was the first example of a cube-shaped SMM cluster and the first SMM containing $5d$ electrons. Table 4 lists some examples of SMMs.

In summary, SMMs have uniform size, readily alterable peripheral ligands and solubility in organic solvents. These properties are not easy to obtain for conventional magnetic recording materials composed of metals, metal oxides or metal alloys. The slow relaxation of the magnetization in SMMs can be applied in data storage as the direction of spin in individual molecules representing “0” and “1” states. To stabilize this bistability, SMMs with larger S values and more negative D values are strongly

Table 4. Examples of single molecule magnets and their properties.

Formula	<i>S</i>	<i>D</i> (cm ⁻¹)	<i>U</i> _{eff} (cm ⁻¹)	Reference
[Mn ₁₂ O ₁₂ (O ₂ CCH ₃) ₁₆ (H ₂ O) ₄]	10	-0.5	42	166
[Fe ₈ O ₂ (OH) ₁₂ (tacn) ₆] ⁸⁺	10	-0.19	15	169
[Mn ₈₄ O ₇₂ (O ₂ CCH ₃) ₇₈ (OCH ₃) ₂₄ (CH ₃ OH) ₁₂ (H ₂ O) ₄₂ (OH) ₆]	—	—	—	171
[Mn ₁₂ O ₁₂ (O ₂ CCHCl ₂) ₁₆ (H ₂ O) ₄][PPh ₄] ₂	10	-0.27	27*	173
[Mn ₁₂ O ₁₂ (O ₂ C-p-CH ₃ C ₆ H ₄) ₁₆ (H ₂ O) ₄]	—	—	—	174
[Mn ₁₂ O ₁₂ (O ₂ CCH ₃) ₈ (O ₂ PPh ₂) ₈ (H ₂ O) ₄]	10	-0.41	42	175
[Mn ₄ (O ₂ CCH ₃) ₂ (pdmH) ₆](ClO ₄) ₂	8	-0.25	12	176
[Mn ₃₀ O ₂₄ (OH) ₈ (O ₂ CCH ₂ Bu') ₃₂ (H ₂ O) ₂ (CH ₃ NO ₂) ₄]	7	-0.79	39	177
[Fe ₁₉ O ₆ (OH) ₁₄ (methedi) ₁₀ (H ₂ O) ₁₂] ⁺	33/2	-0.035	12	178, 179
[Ni ₁₂ (chp) ₁₂ (O ₂ CCH ₃) ₁₂ (H ₂ O) ₆ (THF) ₆]	12	-0.047	7	180, 181
[{MnCl} ₄ {Re-(triphos)(CN) ₃ } ₄]	8	-0.39	8.8	172

tacn = 1,4,7-triazacyclononane

pdmH = pyridine-2,6-dimethanol

methediH₃ = *N*-(1-hydroxynethyl)iminodiacetic acid

chp = 6-chloro-2-pyridonate

triphos = 1,1,1-tris(diphenylphosphinomethyl)ethane

*Estimated value, $U = S^2|D|$

5f21ac93d18f02ae446bef93ae6067dc

ebrary

needed. Numerous synthetic strategies aimed at the improvement of these materials have been considered. It is well known that the minimum dimension of a single recording bit is limited by the onset of superparamagnetism. In SMMs, magnetic properties are due only to intramolecular rather than intermolecular interactions. Each single molecule acts as a tiny magnet and stores one bit. This implies a 10,000 times greater storage density capacity than that of the best current computer manufacturers.¹⁸²

5. Summary

This chapter provides a broad summary of recent research activities in the area of ultrahigh density magnetic recording. Perpendicular

5f21ac93d18f02ae446bef93ae6067dc

ebrary

recording has been explored as the closest alternative to longitudinal recording, where the write head field is enhanced by the combination of a single pole write head and a soft underlayer. Patterned media provides a new way to further increase the storage density and reduce the media noise by lithographic definition of the recording transitions, hence enabling recording with one or several grains per bit. However, advanced nanolithography technologies were limited by high cost and low resolution.

To further decrease the grain size and reduce the cost of preparing patterned nanoparticles, synthesis of magnetic nanoparticles and the self-assembly method are proposed as a promising alternative. However, there are still a number of new problems to be resolved before extensive application, such as the control of the surface roughness, the orientation of the easy axis and the repeatability of the large scale manufacture.

Organic groups in organic and molecular magnets provide new sources of magnetic moments or mediate magnetic exchange interaction, which present several attributes unavailable in conventional inorganic magnets. A self-assembled monolayer of single molecule magnets may be used as a recording medium in the future by storing a single bit in an individual molecule. It will lead to very high surface storage density, since each molecule is only 1–2 nm in diameter. However, it remains a tremendous challenge to read and write on bits with such small magnetic moments.

In a word, superparamagnetic effect is the limitation on magnetic data storage, but the onset can be delayed by using different recording techniques. It is believed that ultrahigh density magnetic recording will be realized by replacing conventional longitudinal magnetic data storage with other alternative methods. Before this comes to fruition, further experimental and theoretical work is required to develop all of these possible methods.

Acknowledgments

The authors thank the Natural Science Foundation of China (NSFC), the Ministry of Science and Technology of China (MOST), and the Chinese

Academy of Sciences (CAS) for continuous financial support. The National Sciences Fund for Distinguished Young Scholars is especially acknowledged.

References

1. S. X. Wang and A. M. Taratorin, *Magnetic Information Storage Technology* (Academic Press, Boston, 1999), pp. 10–11.
2. http://www.hitachigst.com/hdd/research/recording_head/pr/index.html
3. S. H. Charap, P. L. Lu and Y. J. He, Thermal stability of recorded information at high densities, *IEEE Trans. Magn.* **33**, 978–983 (1997).
4. H. N. Bertram, X. B. Wang and V. L. Safonov, Dynamic-thermal effects in thin film media, *IEEE Trans. Magn.* **37**, 1521–1527 (2001).
5. J. D. Livingston, A review of coercivity mechanisms, *J. Appl. Phys.* **52**, 2544–2548 (1981).
6. G. Bertotti, *Hysteresis in Magnetism* (Academic Press, San Diego, 1998).
7. R. L. Comstock, *Introduction to Magnetism and Magnetic Recording* (John Wiley & Sons, 1999).
8. E. Clark, *Magnetostriuctive Rare Earth–Fe₂ Compounds in Ferromagnetic Materials*, ed. E. P. Wolfarth (North-Holland, 1980).
9. D. A. Thompson and J. S. Best, The future of magnetic data storage technology, *IBM J. Res. Develop.* **44**, 311–322 (2000).
10. H. Kodama, S. Momose, T. Sugimoto, T. Uzumaki and A. Tanaka, Chemically synthesized FePt nanoparticle material for ultrahigh-density recording, *IEEE Trans. Magn.* **41**, 665–669 (2005).
11. D. Shriver and P. Atkins, *Inorganic Chemistry*, 3rd edn. (Oxford University Press, 1999).
12. J. H. V. Vleck, *The Theory of Electric and Magnetic Susceptibilities* (Oxford University Press, 1932).
13. J. H. V. Vleck, http://nobelprize.org/nobel_prizes/physics/laureates/1977/vleck-lecture.pdf
14. A. Moser, K. Takano, D. T. Margulies, M. Albrecht, Y. Sonobe, Y. Ikeda, S. H. Sun and E. E. Fullerton, Magnetic recording: advancing into the future, *J. Phys. D* **35**, R157–R167 (2002).
15. M. N. Baibich, J. M. Broto, A. Fert, F. N. Vandau, F. Petroff, P. Eitenne, G. Creuzet, A. Friederich and J. Chazelas, Giant magnetoresistance of

- (001)Fe/(001)Cr magnetic superlattices, *Phys. Rev. Lett.* **61**, 2472–2475 (1988).
16. S. S. P. Parkin, Z. G. Li and D. J. Smith, Giant magnetoresistance in anti-ferromagnetic Co/Cu multilayers, *Appl. Phys. Lett.* **58**, 2710–2712 (1991).
 17. <http://www.stoner.leeds.ac.uk/research/gmr.htm>
 18. Y. C. Feng, D. E. Laughlin and D. N. Lambeth, Formation of crystallographic texture in Rf sputter-deposited Cr thin films, *J. Appl. Phys.* **76**, 7311–7316 (1994).
 19. P. J. Grundy, Thin film magnetic recording media, *J. Phys. D* **31**, 2975–2990 (1998).
 20. A. Ross, T. P. Nolan, R. Ranjan and D. Lu, The role of NiAl under-layers in longitudinal thin-film recording media, *J. Appl. Phys.* **81**, 7441–7444 (1997).
 21. R. L. Comstock, *Introduction to Magnetism and Magnetic Recording* (John Wiley & Sons, 1999), pp. 419–432.
 22. B. Lu and D. E. Laughlin, Microstructure of longitudinal media, in *The Physics of Ultra-High-Density Magnetic Recording*, eds. M. L. Plumer, J. van Ek and D. Weller (Springer, 2002), pp. 34–80.
 23. D. Weller and A. Moser, Thermal effect limits in ultrahigh-density magnetic recording, *IEEE Trans. Magn.* **35**, 4423–4439 (1999).
 24. R. Wood, The feasibility of magnetic recording at 1 terabit per square inch, *IEEE Trans. Magn.* **36**, 36–42 (2000).
 25. A. Moser, D. Weller and M. F. Doerner, Thermal stability of longitudinal magnetic recording media, *Appl. Phys. Lett.* **75**, 1604–1606 (1999).
 26. M. F. Doerner, K. Tang, T. Arnoldussen, H. Zeng, M. F. Toney and D. Weller, Microstructure and thermal stability of advanced longitudinal media, *IEEE Trans. Magn.* **36**, 43–47 (2000).
 27. D. Weller, A. Moser, L. Folks, M. E. Best, W. Lee, M. F. Toney, M. Schwickert, J. U. Thiele and M. F. Doerner, High K_u materials approach to 100 Gbits/in², *IEEE Trans. Magn.* **36**, 10–15 (2000).
 28. J. H. Judy, Advancements in PMR thin-film media, *J. Magn. Magn. Mater.* **287**, 16–26 (2005).
 29. C. Fery, L. Hennet, O. Lenoble, M. Piecuch, E. Snoeck and J. F. Bobo, Magnetic tunnelling in Fe–Al₂O₃–Fe trilayers with radio-frequency sputtered Al₂O₃ barrier layers, *J. Phys.: Condens. Matter* **10**, 6629–6642 (1998).

30. S. Iwasaki and K. Takemura, Analysis for circular mode of magnetization in short wavelength recording, *IEEE Trans. Magn.* **11**, 1173–1175 (1975).
31. S. Iwasaki and Y. Nakamura, Analysis for magnetization mode for high-density magnetic recording, *IEEE Trans. Magn.* **13**, 1272–1277 (1977).
32. R. H. Victora, J. H. Xue and M. Patwari, Areal density limits for perpendicular magnetic recording, *IEEE Trans. Magn.* **38**, 1886–1891 (2002).
33. S. Iwasaki, Guiding principle for research on perpendicular magnetic recording, *IEEE Trans. Magn.* **41**, 683–686 (2005).
34. D. Litvinov and S. Khizroev, Perpendicular magnetic recording: playback, *J. Appl. Phys.* **97**, 071101 (2005).
35. S. Iwasaki and K. Ouchi, Co–Cr recording films with perpendicular magnetic anisotropy, *IEEE Trans. Magn.* **14**, 849–851 (1978).
36. S. Iwasaki, Y. Nakamura and K. Ouchi, Perpendicular magnetic recording with a composite anisotropy film, *IEEE Trans. Magn.* **15**, 1456–1458 (1979).
37. M. H. Kryder, W. Messner and L. R. Carley, Approaches to 10 Gbit/in² recording, *J. Appl. Phys.* **79**, 4485–4490 (1996).
38. Y. Nakamura, S. Yamamoto and S. Iwasaki, The effect of magnetic interaction between medium and head on perpendicular magnetic recording characteristics, *IEEE Trans. Magn.* **22**, 376–378 (1986).
39. Y. Nakamura, Basic design concepts for perpendicular magnetic recording — from viewpoints of high writing ability and resolution, *J. Magn. Magn. Mater.* **287**, 27–40 (2005).
40. S. Iwasaki and Y. Nakamura, Magnetic-field distribution of a perpendicular recording head, *IEEE Trans. Magn.* **14**, 436–438 (1978).
41. D. Litvinov, M. H. Kryder and S. Khizroev, Recording physics of perpendicular media: hard layers, *J. Magn. Magn. Mater.* **241**, 453–465 (2002).
42. S. Khizroev and D. Litvinov, *Perpendicular Magnetic Recording* (Kluwer, 2004).
43. T. Suzuki, T. Kiya, N. Honda and K. Ouchi, FePt perpendicular double-layered media with high recording resolution, *J. Magn. Magn. Mater.* **235**, 312–318 (2001).
44. K. Takano, G. Zeltzer, D. K. Weller and E. E. Fullerton, Co_{1-x}Cr_x/Pt multilayers as perpendicular recording media, *J. Appl. Phys.* **87**, 6364–6366 (2000).

45. G. Roy, D. E. Laughlin, T. J. Klemmer, K. Howard, S. Khizroev and D. Litvinov, Seed-layer effect on the microstructure and magnetic properties of Co/Pd multilayers, *J. Appl. Phys.* **89**, 7531–7533 (2001).
46. S. Iwasaki, Perpendicular magnetic recording, *IEEE Trans. Magn.* **16**, 71–76 (1980).
47. S. Iwasaki, Principal complementarity between perpendicular and longitudinal magnetic recording, *J. Magn. Magn. Mater.* **287**, 9–15 (2005).
48. Y. Y. Zou, J. P. Wang, C. H. Hee and T. C. Chong, Tilted media in a perpendicular recording system for high areal density recording, *Appl. Phys. Lett.* **82**, 2473–2475 (2003).
49. J. P. Wang, Y. Y. Zou, C. H. Hee, T. C. Chong and Y. F. Zheng, Approaches to tilted magnetic recording for extremely high areal density, *IEEE Trans. Magn.* **39**, 1930–1935 (2003).
50. T. W. McDaniel, Ultimate limits to thermally assisted magnetic recording, *J. Phys.: Condens. Matter* **17**, R315–R332 (2005).
51. C. Ross, Patterned magnetic recording media, *Ann. Rev. Mater. Res.* **31**, 203–235 (2001).
52. R. L. White, R. M. H. New and R. F. W. Pease, Patterned media: a viable route to 50 Gbit/in² and up for magnetic recording? *IEEE Trans. Magn.* **33**, 990–995 (1997).
53. O. Dial, C. C. Cheng and A. Scherer, Fabrication of high-density nanostructures by electron beam lithography, *J. Vac. Sci. Technol. B* **16**, 3887–3890 (1998).
54. A. Ross, H. I. Smith, T. Savas, M. Schattenburg, M. Farhoud, M. Hwang, M. Walsh, M. C. Abraham and R. J. Ram, Fabrication of patterned media for high density magnetic storage, *J. Vac. Sci. Technol. B* **17**, 3168–3176 (1999).
55. J. C. Lodder, Methods for preparing patterned media for high-density recording, *J. Magn. Magn. Mater.* **272–276**, 1692–1697 (2004).
56. J. I. Martin, J. Nogues, K. Liu, J. L. Vicent and I. K. Schuller, Ordered magnetic nanostructures: fabrication and properties, *J. Magn. Magn. Mater.* **256**, 449–501 (2003).
57. B. D. Terris and T. Thomson, Nanofabricated and self-assembled magnetic structures as data storage media, *J. Phys. D* **38**, R199–R222 (2005).
58. *Handbook of Microlithography, Micromachining, and Microfabrication*, ed. P. Rai-Choudhury, Bellingham, Washington, USA (SPIE Optical Engineering Press, London; Institution of Electrical Engineers, 1997).

59. S. Y. Chou, P. R. Krauss and P. J. Renstrom, Nanoimprint lithography, *J. Vac. Sci. Technol. B* **14**, 4129–4133 (1996).
60. S. Y. Chou, P. R. Krauss and P. J. Renstrom, Imprint lithography with 25-nanometer resolution, *Science* **272**, 85–87 (1996).
61. J. M. Carter, R. C. Fleming, T. A. Savas, M. E. Walsh and T. B. O'Reilly, Interference lithography, *MTL Annual Report* (2003).
62. T. A. Savas, S. N. Shah, M. L. Schattenburg, J. M. Carter and H. I. Smith, Achromatic interferometric lithography for 100-nm-period gratings and grids, *J. Vac. Sci. Technol. B* **13**, 2732–2735 (1995).
63. T. A. Savas, M. L. Schattenburg, J. M. Carter and H. I. Smith, Large-area achromatic interferometric lithography for 100 nm period gratings and grids, *J. Vac. Sci. Technol. B* **14**, 4167–4170 (1996).
64. T. A. Savas, M. Farhoud, H. I. Smith, M. Hwang and C. A. Ross, Properties of large-area nanomagnet arrays with 100 nm period made by interferometric lithography, *J. Appl. Phys.* **85**, 6160–6162 (1999).
65. I. W. Hamley, Nanostructure fabrication using block copolymers, *Nanotechnology* **14**, R39–R54 (2003).
66. P. Mansky, P. Chaikin and E. L. Thomas, Monolayer films of diblock copolymer microdomains for nanolithographic applications, *J. Mater. Sci.* **30**, 1987–1992 (1995).
67. R. R. Li, P. D. Dapkus, M. E. Thompson, W. G. Jeong, C. Harrison, P. M. Chaikin, R. A. Register and D. H. Adamson, Dense arrays of ordered GaAs nanostructures by selective area growth on substrates patterned by block copolymer lithography, *Appl. Phys. Lett.* **76**, 1689–1691 (2000).
68. T. Thurn-Albrecht, R. Steiner, J. DeRouchey, C. M. Stafford, E. Huang, M. Bal, M. Tuominen, C. J. Hawker and T. Russell, Nanoscopic templates from oriented block copolymer films, *Adv. Mater.* **12**, 787–791 (2000).
69. Y. Cheng, C. A. Ross, V. Z. H. Chan, E. L. Thomas, R. G. H. Lammertink and G. J. Vancso, Formation of a cobalt magnetic dot array via block copolymer lithography, *Adv. Mater.* **13**, 1174–1178 (2001).
70. Y. Cheng, C. A. Ross, E. L. Thomas, H. I. Smith and G. J. Vancso, Templated self-assembly of block copolymers: effect of substrate topography, *Adv. Mater.* **15**, 1599–1602 (2003).
71. J. Fasolka, D. J. Harris, A. M. Mayes, M. Yoon and S. G. J. Mochrie, Observed substrate topography-mediated lateral patterning of diblock copolymer films, *Phys. Rev. Lett.* **79**, 3018–3021 (1997).

72. J. Y. Cheng, A. M. Mayes and C. A. Ross, Nanostructure engineering by templated self-assembly of block copolymers, *Nat. Mater.* **3**, 823–828 (2004).
73. X. M. Yang, R. D. Peters, P. F. Nealey, H. H. Solak and F. Cerrina, Guided self-assembly of symmetric diblock copolymer films on chemically nanopatterned substrates, *Macromolecules* **33**, 9575–9582 (2000).
74. C. De Rosa, C. Park, E. L. Thomas and B. Lotz, Micro-domain patterns from directional eutectic solidification and epitaxy, *Nature* **405**, 433–437 (2000).
75. S. Palacin, P. C. Hidber, J. P. Bourgoin, C. Miramond, C. Fermon and G. M. Whitesides, Patterning with magnetic materials at the micron scale, *Chem. Mater.* **8**, 1316–1325 (1996).
76. K. Naito, H. Hieda, M. Sakurai, Y. Kamata and K. Asakawa, 2.5-inch disk patterned media prepared by an artificially assisted self-assembling method, *IEEE Trans. Magn.* **38**, 1949–1951 (2002).
77. T. Thurn-Albrecht, J. Schotter, C. A. Kastle, N. Emley, T. Shibauchi, L. Krusin-Elbaum, K. Guarini, C. T. Black, M. T. Tuominen and T. P. Russell, Ultrahigh-density nanowire arrays grown in self-assembled diblock copolymer templates, *Science* **290**, 2126–2129 (2000).
78. C. T. Rettner, M. E. Best and B. D. Terris, Patterning of granular magnetic media with a focused ion beam to produce single-domain islands at > 140 Gbit/in², *IEEE Trans. Magn.* **37**, 1649–1651 (2001).
79. A. Dietzel, R. Berger, H. Grimm, W. H. Bruenger, C. Dzionk, F. Letzkus, R. Springer, H. Loeschner, E. Platzgummer, G. Stengl, Z. Z. Bandic and B. D. Terris, Ion projection direct structuring for patterning of magnetic media, *IEEE Trans. Magn.* **38**, 1952–1954 (2002).
80. A. Dietzel, R. Berger, H. Loeschner, E. Platzgummer, G. Stengl, W. H. Bruenger and F. Letzkus, Nanopatterning of magnetic disks by single-step Ar⁺ ion projection, *Adv. Mater.* **15**, 1152–1155 (2003).
81. J. Fassbender, D. Ravelosona and Y. Samson, Tailoring magnetism by light-ion irradiation, *J. Phys. D* **37**, R179–R196 (2004).
82. B. D. Cullity, *Introduction to Magnetic Materials* (Addison-Wesley, Reading, Massachusetts, 1972), p. 387.
83. T. Yogi and T. A. Nguyen, Ultra-high-density media — gigabit and beyond, *IEEE Trans. Magn.* **29**, 307–316 (1993).
84. X. W. Teng and H. Yang, Synthesis of face-centered tetragonal FePt nanoparticles and granular films from Pt@Fe₂O₃ core-shell nanoparticles, *J. Am. Chem. Soc.* **125**, 14559–14563 (2003).

85. C. Haginoya, K. Koike, Y. Hirayama, J. Yamamoto, M. Ishibashi, O. Kitakami and Y. Shimada, Thermomagnetic writing on 29 Gbit/in² patterned magnetic media, *Appl. Phys. Lett.* **75**, 3159–3161 (1999).
86. P. Vettiger, M. Despont, U. Drechsler, U. Dürig, W. Häberle, M. I. Lutwyche, H. E. Rothuizen, R. Stutz, R. Widmer and G. K. Binnig, The “Millipede” — more than one thousand tips for future AFM data storage, *IBM J. Res. Develop.* **44**, 323–340 (2000).
87. A. Moser, D. Weller, M. E. Best and M. F. Doerner, Dynamic coercivity measurements in thin film recording media using a contact write/read tester, *J. Appl. Phys.* **85**, 5018–5020 (1999).
88. M. Albrecht, C. T. Rettner, A. Moser, M. E. Best and B. D. Terris, Recording performance of high-density patterned perpendicular magnetic media, *Appl. Phys. Lett.* **81**, 2875–2877 (2002).
89. M. Albrecht, S. Ganesan, C. T. Rettner, A. Moser, M. E. Best, R. L. White and B. D. Terris, Patterned perpendicular and longitudinal media: a magnetic recording study, *IEEE Trans. Magn.* **39**, 2323–2325 (2003).
90. S. Sun, D. Weller, and C. B. Murray, The physics of ultra-high-density magnetic recording, in *Self-Assembled Magnetic Nanoparticle Arrays*, eds. M. L. Plumer, J. van Ek and D. Weller (Springer, New York, 2001) p. 249.
91. T. Black, C. B. Murray, R. L. Sandstrom and S. H. Sun, Spin-dependent tunneling in self-assembled cobalt-nanocrystal superlattices, *Science* **290**, 1131–1134 (2000).
92. S. H. Sun, C. B. Murray, D. Weller, L. Folks and A. Moser, Monodisperse FePt nanoparticles and ferromagnetic FePt nanocrystal superlattices, *Science* **287**, 1989–1992 (2000).
93. Y. L. Hou, H. Kondoh, T. Kogure and T. Ohta, Preparation and characterization of monodisperse FePd nanoparticles, *Chem. Mater.* **16**, 5149–5152 (2004).
94. S. H. Sun, H. Zeng, D. B. Robinson, S. Raoux, P. M. Rice, S. X. Wang and G. X. Li, Monodisperse MFe₂O₄ (M = Fe, Co, Mn) nanoparticles, *J. Am. Chem. Soc.* **126**, 273–279 (2004).
95. H. Zeng, P. M. Rice, S. X. Wang and S. H. Sun, Shape-controlled synthesis and shape-induced texture of MnFe₂O₄ nanoparticles, *J. Am. Chem. Soc.* **126**, 11458–11459 (2004).
96. S. H. Sun, S. Anders, T. Thomson, J. E. E. Baglin, M. F. Toney, H. F. Hamann, C. B. Murray and B. D. Terris, Controlled synthesis and assembly of FePt nanoparticles, *J. Phys. Chem. B* **107**, 5419–5425 (2003).

97. C. Liu, X. W. Wu, T. Klemmer, N. Shukla, X. M. Yang, D. Weller, A. G. Roy, M. Tanase and D. Laughlin, Polyol process synthesis of monodisperse FePt nanoparticles, *J. Phys. Chem. B* **108**, 6121–6123 (2004).
98. S. H. Sun, E. E. Fullerton, D. Weller and C. B. Murray, Compositionally controlled FePt nanoparticle materials, *IEEE Trans. Magn.* **37**, 1239–1243 (2001).
99. K. E. Elkins, T. S. Vedantam, J. P. Liu, H. Zeng, S. H. Sun, Y. Ding and Z. L. Wang, Ultrafine FePt nanoparticles prepared by the chemical reduction method, *Nano Lett.* **3**, 1647–1649 (2003).
100. M. Chen, J. P. Liu and S. H. Sun, One-step synthesis of FePt nanoparticles with tunable size, *J. Am. Chem. Soc.* **126**, 8394–8395 (2004).
101. Z. R. Dai, S. H. Sun and Z. L. Wang, Phase transformation, coalescence, and twinning of monodispersed FePt nanocrystals, *Nano Lett.* **1**, 443–447 (2001).
102. T. Thomson, M. F. Toney, S. Raoux, S. L. Lee, S. Sun, C. B. Murray and B. D. Terris, Structural and magnetic model of self-assembled FePt nanoparticle arrays, *J. Appl. Phys.* **96**, 1197–1201 (2004).
103. S. Kang, J. W. Harrell and D. E. Nikles, Reduction of the fcc to $L1_0$ ordering temperature for self-assembled FePt nanoparticles containing Ag, *Nano Lett.* **2**, 1033–1036 (2002).
104. M. Chen and D. E. Nikles, Synthesis, self-assembly, and magnetic properties of $Fe_xCo_yPt_{100-x-y}$ nanoparticles, *Nano Lett.* **2**, 211–214 (2002).
105. B. Rellinghaus, S. Stappert, M. Acet and E. F. Wassermann, Magnetic properties of FePt nanoparticles, *J. Magn. Magn. Mater.* **266**, 142–154 (2003).
106. H. G. Boyen, K. Fauth, B. Stahl, P. Ziemann, G. Kastle, F. Weigl, F. Banhart, M. Hessler, G. Schutz, N. S. Gajbhiye, J. Ellrich, H. Hahn, M. Buttner, M. G. Garnier and P. Oelhafen, Electronic and magnetic properties of ligand-free FePt nanoparticles, *Adv. Mater.* **17**, 574–578 (2005).
107. C. R. Vestal and Z. J. Zhang, Effects of surface coordination chemistry on the magnetic properties of $MnFe_2O_4$ spinel ferrite nanoparticles, *J. Am. Chem. Soc.* **125**, 9828–9833 (2003).
108. A. Mayes, A. Bewick, D. Gleeson, J. Hoinville, R. Jones, O. Kasyutich, A. Nartowski, B. Warne, J. Wiggins and K. K. W. Wong, Biologically derived nanomagnets in self-organized patterned media, *IEEE Trans. Magn.* **39**, 624–627 (2003).

109. B. D. Reiss, C. B. Mao, D. J. Solis, K. S. Ryan, T. Thomson and A. M. Belcher, Biological routes to metal alloy ferromagnetic nanostructures, *Nano Lett.* **4**, 1127–1132 (2004).
110. Y. P. Bao, M. Beerman and K. M. Krishnan, Controlled self-assembly of colloidal cobalt nanocrystals, *J. Magn. Magn. Mater.* **266**, L245–L249 (2003).
111. S. H. Sun, S. Anders, H. F. Hamann, J. U. Thiele, J. E. E. Baglin, T. Thomson, E. E. Fullerton, C. B. Murray and B. D. Terris, Polymer mediated self-assembly of magnetic nanoparticles, *J. Am. Chem. Soc.* **124**, 2884–2885 (2002).
112. A. Braun, Y. Eichen, U. Sivan and G. Ben-Yoseph, DNA-templated assembly and electrode attachment of a conducting silver wire, *Nature* **391**, 775–778 (1998).
113. S. R. Whaley, D. S. English, E. L. Hu, P. F. Barbara and A. M. Belcher, Selection of peptides with semiconductor binding specificity for directed nanocrystal assembly, *Nature* **405**, 665–668 (2000).
114. Q. J. Guo, X. W. Teng, S. Rahman and H. Yang, Patterned Langmuir–Blodgett films of monodispersed nanoparticles of iron oxide using soft lithography, *J. Am. Chem. Soc.* **125**, 630–631 (2003).
115. J. S. Miller and A. J. Epstein, Molecule-based magnets — an overview, *MRS Bull.* **25**, 21–28 (2000).
116. T. S. Mark, M. Turnbull and L. K. Thompson, *Molecule-Based Magnetic Materials: Theory, Techniques, and Applications* (American Chemical Society, 1996).
117. M. Tamura, Y. Nakazawa, D. Shiomi, K. Nozawa, Y. Hosokoshi, M. Ishikawa, M. Takahashi and M. Kinoshita, Bulk ferromagnetism in the beta-phase crystal of the para-nitrophenyl nitronyl nitroxide radical, *Chem. Phys. Lett.* **186**, 401–404 (1991).
118. J. M. Rawson and F. Palacio, Magnetic properties of thiacyl radicals, (pi)-electron magnetism from molecules to magnetic materials, *Struct. Bond.* **100**, 93–128 (2001).
119. F. Palacio, E. Ressouche and J. Schweizer, *Introduction to Physical Techniques in Molecular Magnetism: Structural and Macroscopic Techniques* (University of Zaragoza, Spain, 2001).
120. A. M. McConnell, Ferromagnetism in solid free radicals, *J. Chem. Phys.* **39**, 1910–1911 (1963).

121. M. McConnell, Proc. Robert A. Welch Foundation, *Chem. Res.* **11**, 144–154 (1967).
122. J. Azuma, The magnetic properties of verdazyl free radicals. 14: Relation between exchange interaction and crystal structure of verdazyl radicals — as studied by means of McConnell spin density Hamiltonian, *Bull. Chem. Soc. Jpn.* **55**, 1357–1361 (1982).
123. A. Zheludev, M. Bonnet, E. Ressouche, J. Schweizer, M. X. Wang and H. L. Wang, Experimental spin density in the 1st purely organic ferromagnet — the beta-para-nitrophenyl nitronyl nitroxide, *J. Magn. Magn. Mater.* **135**, 147–160 (1994).
124. T. Nogami, K. Tomioka, T. Ishida, H. Yoshikawa, M. Yasui, F. Iwasaki, H. Iwamura, N. Takeda and M. Ishikawa, A new organic ferromagnet — 4-benzylideneamino-2,2,6,6-tetramethylpiperidin-1-oxyl, *Chem. Lett.* 29–32 (1994).
125. T. Nogami, T. Ishida, M. Yasui, F. Iwasaki, N. Takeda, M. Ishikawa, T. Kawakami and K. Yamaguchi, Proposed mechanism of ferromagnetic interaction of organic ferromagnets: 4-(arylmethyleneamino)-2,2,6,6-tetramethylpiperidin-1-oxyls and related compounds, *Bull. Chem. Soc. Jpn.* **69**, 1841–1848 (1996).
126. R. Chiarelli, M. A. Novak, A. Rassat and J. L. Tholence, A ferromagnetic transition at 1.48 K in an organic nitroxide, *Nature* **363**, 147–149 (1993).
127. Y. Hosokoshi, K. Katoh, Y. Nakazawa, H. Nakano and K. Inoue, Approach to a single-component ferrimagnetism by organic radical crystals, *J. Am. Chem. Soc.* **123**, 7921–7922 (2001).
128. K. Takeda, T. Hamano, T. Kawae, M. Hidaka, M. Takahashi, S. Kawasaki and K. Mukai, Experimental check of Heisenberg chain quantum statistics for a ferromagnetic organic radical crystal, *J. Phys. Soc. Jpn.* **64**, 2343–2346 (1995).
129. B. Palacio, G. Antorrena, M. Castro, R. Burriel, J. Rawson, J. N. B. Smith, N. Bricklebank, J. Novoa and C. Ritter, High-temperature magnetic ordering in a new organic magnet, *Phys. Rev. Lett.* **79**, 2336–2339 (1997).
130. W. Fujita and K. Awaga, Room-temperature magnetic bistability in organic radical crystals, *Science* **286**, 261–262 (1999).
131. J. M. Allemand, K. C. Khemani, A. Koch, F. Wudl, K. Holczer, S. Donovan, G. Gruner and J. D. Thompson, Organic molecular soft ferromagnetism in a fullerene-C₆₀, *Science* **253**, 301–303 (1991).

132. B. Narymbetov, A. Omerzu, V. V. Kabanov, M. Tokumoto, H. Kobayashi and D. Mihailovic, Origin of ferromagnetic exchange interactions in a fullerene-organic compound, *Nature* **407**, 883–885 (2000).
133. A. Mrzel, A. Omerzu, P. Umek, D. Mihailovic, Z. Jaglicic and Z. Trontelj, Ferromagnetism in a cobaltocene-doped fullerene derivative below 19 K due to unpaired spins only on fullerene molecules, *Chem. Phys. Lett.* **298**, 329–334 (1998).
134. T. L. Makarova, B. Sundqvist, R. Hohne, P. Esquinazi, Y. Kopelevich, P. Scharff, V. A. Davydov, L. S. Kashevarova and A. V. Rakhmanina, Magnetic carbon, *Nature* **413**, 716–718 (2001).
135. V. N. Narozhnyi, K. H. Muller, D. Eckert, A. Teresiak, L. Dunsch, V. A. Davydov, S. Kashevarova and A. V. Rakhmanina, Ferromagnetic carbon with enhanced Curie temperature, *Phys. B: Condens. Matter* **329**, 1217–1218 (2003).
136. V. E. Antonov, I. O. Bashkin, S. S. Khasanov, A. P. Moravsky, Y. G. Morozov, Y. M. Shulga, Y. A. Ossipyan and E. G. Ponyatovsky, Magnetic ordering in hydrofullerite $C_{60}H_{24}$, *J. Alloys Compound* **330**, 365–368 (2002).
137. D. W. Boukhvalov, P. F. Karimov, E. Z. Kurmaev, T. Hamilton, A. Moewes, L. D. Finkelstein, M. I. Katsnelson, V. A. Davydov, A. V. Rakhmanina, T. L. Makarova, Y. Kopelevich, S. Chiuzbaian and M. Neumann, Testing the magnetism of polymerized fullerene, *Phys. Rev. B* **69**, 115425–115428 (2004).
138. A. Chan, B. Montanari, J. D. Gale, S. M. Bennington, J. W. Taylor and N. M. Harrison, Magnetic properties of polymerized C_{60} : the influence of defects and hydrogen, *Phys. Rev. B* **70**, 041403–041406 (2004).
139. A. S. Miller, J. C. Calabrese, H. Rommelmann, S. R. Chittipeddi, J. H. Zhang, W. M. Reiff and A. J. Epstein, Ferromagnetic behavior of $[Fe(C_5Me_5)_2]^{+}[TCNE]^{-}$. Structural and magnetic characterization of decamethylferrocenium tetracyanoethenide, $[Fe(C_5Me_5)_2]^{+}[TCNE]^{-}$, MeCN, and decamethylferrocenium pentacyanopropenide, $[Fe(C_5Me_5)_2]^{+}[C_3(CN)_5]^{-}$, *J. Am. Chem. Soc.* **109**, 769–781 (1987).
140. B. T. Yee, J. M. Manriquez, D. A. Dixon, R. S. Mclean, D. M. Groski, R. B. Flippen, K. S. Narayan, A. J. Epstein and J. S. Miller, Decamethyl-manganocenium tetracyanoethenide $[Mn(C_5Me_5)_2]^{+}[TCNE]^{-}$ — a molecular ferromagnet with an 8.8 K T_C , *Adv. Mater.* **3**, 309–311 (1991).

141. A. S. Miller, R. S. Mclean, C. Vazquez, J. C. Calabrese, F. L. Zuo and A. J. Epstein, Decamethylchromoceneum tetracyanoethenide $[\text{Cr}(\text{C}_5\text{Me}_5)_2]^{+} [\text{TCNE}]^{-}$: a molecular ferromagnet with $T_c = 3.65$ K, *J. Mater. Chem.* **3**, 215–218 (1993).
142. J. S. Miller and A. J. Epstein, Organic and organometallic molecular magnetic materials — designer magnets, *Angew. Chem. Int. Ed.* **33**, 385–415 (1994).
143. S. Chittipeddi, K. R. Cromack, J. S. Miller and A. J. Epstein, Ferromagnetism in molecular decamethylferroceneum tetracyanoethenide (DMEFC TCNE), *Phys. Rev. Lett.* **58**, 2695–2698 (1987).
144. A. Sinzger, S. Hunig, M. Jopp, D. Bauer, W. Bietsch, J. U. Vonschutz, H. C. Wolf, R. K. Kremer, T. Metzenthin, R. Bau, S. I. Khan, A. Lindbaum, C. L. Lengauer and E. Tillmanns, The organic metal $(\text{Me}_2\text{-DCNQI})_2\text{Cu}$: dramatic changes in solid-state properties and crystal structure due to secondary deuterium effects, *J. Am. Chem. Soc.* **115**, 7696–7705 (1993).
145. J. Kato, H. Kobayashi and A. Kobayashi, Crystal and electronic structures of conductive anion-radical salts $(2,5\text{-R}_1\text{,R}_2\text{-Dcnqi})_2\text{Cu}$ ($\text{DCNQI} = \text{N,N}'\text{-dicyanoquinonediimine}$ — $\text{R}_1, \text{R}_2 = \text{CH}_3, \text{CH}_3\text{O}, \text{Cl}, \text{Br}$), *J. Am. Chem. Soc.* **111**, 5224–5232 (1989).
146. V. Briois, R. M. Lequan, M. Lequan, C. Cartier, G. Vanderlaan, A. Michalowicz and M. Verdaguer, X-ray absorption spectroscopy of Mn, Co, Cu, and Zn inorganic salts of tetrathiafulvalene and bis(ethylenedithio) tetrathiafulvalene, *Chem. Mater.* **4**, 484–493 (1992).
147. A. Umeya, S. Kawata, H. Matsuzaka, S. Kitagawa, H. Nishikawa, K. Kikuchi and I. Ikemoto, X-ray crystal structure, magnetic and electric properties of TTF trimer-based salts of FeCl_4^- , $[\text{TTF}_7(\text{FeCl}_4)_2]$, *J. Mater. Chem.* **8**, 295–300 (1998).
148. K. Inoue, T. Hayamizu, H. Iwamura, D. Hashizume and Y. Ohashi, Assemblage and alignment of the spins of the organic trinitroxide radical with a quartet ground state by means of complexation with magnetic metal ions; a molecule-based magnet with three-dimensional structure and high T_c of 46 K, *J. Am. Chem. Soc.* **118**, 1803–1804 (1996).
149. K. Inoue and H. Iwamura, Ferromagnetic and ferrimagnetic ordering in a 2-dimensional network formed by manganese(II) and 1,3,5-Tris[P(N-tert-butyl-N-oxyamino)phenyl] benzene, *J. Am. Chem. Soc.* **116**, 3173–3174 (1994).

150. J. R. Long, Molecular cluster magnets, in *Chemistry of Nanostructured Materials*, ed. P. Yang (World Scientific, Hong Kong, 2003), p. 299.
151. A. Verdaguer, Rational synthesis of molecular magnetic materials: a tribute to Olivier Kahn, *Polyhedron* **20**, 1115–1128 (2001).
152. Y. Dromzee, R. Chiarelli, S. Gambarelli and A. Rassat, Dupeyredioxyl (1,3,5,7-tetramethyl-2,6-di-azaadamantane-N,N'-dioxyl), *Acta Cryst. C: Cryst. Struct. Commun.* **52**, 474–477 (1996).
153. A. N. Holden, B. T. Matthias, P. W. Anderson and H. W. Lewis, New low-temperature ferromagnets, *Phys. Rev.* **102**, 1463–1463 (1956).
154. V. Gadet, T. Mallah, I. Castro, M. Verdaguer and P. Veillet, High- T_c molecular-based magnets — a ferromagnetic bimetallic chromium(III) nickel(II) cyanide with $T_c = 90$ K, *J. Am. Chem. Soc.* **114**, 9213–9214 (1992).
155. W. D. Griebler and D. Babel, X-ray and magnetic studies of perovskite-related cyano compounds $\text{CsMnIII}(\text{Cn})_6$, *Z. Naturforsch. B* **37**, 832–837 (1982).
156. W. E. Buschmann, S. C. Paulson, C. M. Wynn, M. A. Girtu, A. J. Epstein, H. S. White and J. S. Miller, Magnetic field induced reversed (negative) magnetization for electrochemically deposited $T_c = 260$ K oxidized films of chromium cyanide magnets, *Adv. Mater.* **9**, 645–647 (1997).
157. E. Dujardin, S. Ferlay, X. Phan, C. Desplanches, C. C. D. Moulin, P. Sainctavit, F. Baudelet, E. Dartige, P. Veillet and M. Verdaguer, Synthesis and magnetization of new room-temperature molecule-based magnets: effect of stoichiometry on local magnetic structure by X-ray magnetic circular dichroism, *J. Am. Chem. Soc.* **120**, 11347–11352 (1998).
158. J. Ferlay, T. Mallah, R. Ouahes, P. Veillet and M. Verdaguer, A room-temperature organometallic magnet based on Prussian blue, *Nature* **378**, 701–703 (1995).
159. O. Hatlevik, W. E. Buschmann, J. Zhang, J. L. Manson and J. S. Miller, Enhancement of the magnetic ordering temperature and air stability of a mixed valent vanadium hexacyanochromate(III) magnet to 99 degrees C (372 K), *Adv. Mater.* **11**, 914–918 (1999).
160. J. M. Holmes and G. S. Girolami, Sol-gel synthesis of $\text{KV}^{\text{II}}[\text{Cr}^{\text{III}}(\text{CN})_6] \cdot 2\text{H}_2\text{O}$: a crystalline molecule-based magnet with a magnetic ordering temperature above 100 degrees C, *J. Am. Chem. Soc.* **121**, 5593–5594 (1999).

161. A. E. Chakov, Molecular manganese compounds as single-molecule magnets: a molecular approach to nanoscale magnets, PhD thesis, University of Florida, Gainesville (2005).
162. J. Lis, Preparation, structure, and magnetic properties of a dodecanuclear mixed-valence manganese carboxylate, *Acta Cryst. B: Struct. Sci.* **36**, 2042–2046 (1980).
163. R. Sessoli, H. L. Tsai, A. R. Schake, S. Y. Wang, J. B. Vincent, K. Folting, D. Gatteschi, G. Christou and D. N. Hendrickson, High-spin molecules — $[\text{Mn}_{12}\text{O}_{12}(\text{O}_2\text{Cr})_{16}(\text{H}_2\text{O})_4]$, *J. Am. Chem. Soc.* **115**, 1804–1816 (1993).
164. R. Sessoli, D. Gatteschi, A. Caneschi and M. A. Novak, Magnetic bistability in a metal–ion cluster, *Nature* **365**, 141–143 (1993).
165. L. Thomas, F. Lioni, R. Ballou, D. Gatteschi, R. Sessoli and B. Barbara, Macroscopic quantum tunnelling of magnetization in a single crystal of nanomagnets, *Nature* **383**, 145–147 (1996).
166. R. A. Robinson, P. J. Brown, D. N. Argyriou, D. N. Hendrickson and S. M. J. Aubin, Internal magnetic structure of Mn_{12} acetate by polarized neutron diffraction, *J. Phys.: Condens. Matter* **12**, 2805–2810 (2000).
167. A. J. Eppley, H. L. Tsai, N. Devries, K. Folting, G. Christou and D. N. Hendrickson, High-spin molecules — unusual magnetic-susceptibility relaxation effects in $[\text{Mn}_{12}\text{O}_{12}(\text{O}_2\text{CET})_{16}(\text{H}_2\text{O})_3]$ ($S = 9$) and the one-electron reduction product $(\text{PPh}_4)[\text{Mn}_{12}\text{O}_{12}(\text{O}_2\text{CET})_{16}(\text{H}_2\text{O})_4]$ ($S = 19/2$), *J. Am. Chem. Soc.* **117**, 301–317 (1995).
168. M. R. Cheesman, V. S. Oganesyan, R. Sessoli, D. Gatteschi and A. J. Thomson, Magnetically induced optical bi-stability of the molecular nanomagnet $\text{Mn}_{12}\text{O}_{12}(\text{OOCMe})_{16}(\text{H}_2\text{O})_4$ in an organic glass, *Chem. Commun.* 1677–1678 (1997).
169. C. Sangregorio, T. Ohm, C. Paulsen, R. Sessoli and D. Gatteschi, Quantum tunneling of the magnetization in an iron cluster nanomagnet, *Phys. Rev. Lett.* **78**, 4645–4648 (1997).
170. C. A. A. J. Perenboom, J. S. Brooks, S. Hill, T. Hathaway and N. S. Dalal, Relaxation of the magnetization of Mn-12 acetate, *Phys. Rev. B* **58**, 330–338 (1998).
171. A. J. Tasiopoulos, A. Vinslava, W. Wernsdorfer, K. A. Abboud and G. Christou, Giant single-molecule magnets: a {Mn-84} torus and its

- supramolecular nanotubes, *Angew. Chem. Int. Ed.* **43**, 2117–2121 (2004).
172. E. J. Schelter, A. V. Prosvirin and K. R. Dunbar, Molecular cube of Re-II and Mn-II that exhibits single-molecule magnetism, *J. Am. Chem. Soc.* **126**, 15004–15005 (2004).
173. M. Soler, S. K. Chandra, D. Ruiz, E. R. Davidson, D. N. Hendrickson and G. Christou, A third isolated oxidation state for the Mn_{12} family of single-molecule magnets, *Chem. Commun.* 2417–2418 (2000).
174. S. M. J. Aubin, Z. M. Sun, H. J. Eppley, E. M. Rumberger, I. A. Guzei, K. Folting, P. K. Gantzel, A. L. Rheingold, G. Christou and D. N. Hendrickson, Single-molecule magnets: Jahn–Teller isomerism and the origin of two magnetization relaxation processes in Mn_{12} complexes, *Inorg. Chem.* **40**, 2127–2146 (2001).
175. C. Boskovic, M. Pink, J. C. Huffman, D. N. Hendrickson and G. Christou, Single-molecule magnets: ligand-induced core distortion and multiple Jahn–Teller isomerism in $[Mn_{12}O_{12}(O_2CMe)_8(O_2PPh_2)_8(H_2O)_4]$, *J. Am. Chem. Soc.* **123**, 9914–9915 (2001).
176. C. Yoo, E. K. Brechin, A. Yamaguchi, M. Nakano, J. C. Huffman, A. L. Maniero, L. C. Brunel, K. Awaga, H. Ishimoto, G. Christou and D. N. Hendrickson, Single-molecule magnets: a new class of tetranuclear manganese magnets, *Inorg. Chem.* **39**, 3615–3623 (2000).
177. M. Soler, E. Rumberger, K. Folting, D. N. Hendrickson and G. Christou, Synthesis, characterization and magnetic properties of $[Mn_{30}O_{24}(OH)_8(O_2CCH_2C(CH_3)_3)_3(H_2O)_2(CH_3NO_2)_4]$: the largest manganese carboxylate cluster, *Polyhedron* **20**, 1365–1369 (2001).
178. C. C. Goodwin, R. Sessoli, D. Gatteschi, W. Wernsdorfer, A. K. Powell and S. L. Heath, Towards nanostructured arrays of single molecule magnets: new Fe_{19} oxyhydroxide clusters displaying high ground state spins and hysteresis, *J. Chem. Soc.: Dalton Trans.* 1835–1840 (2000).
179. M. Affronte, J. C. Lasjaunias, W. Wernsdorfer, R. Sessoli, D. Gatteschi, S. L. Heath, A. Fort and A. Rettori, Magnetic ordering in a high-spin Fe_{19} molecular nanomagnet, *Phys. Rev. B* **66**, 064408–064414 (2002).
180. C. Cadiou, M. Murrie, C. Paulsen, V. Villar, W. Wernsdorfer and R. E. P. Winpenny, Studies of a nickel-based single molecule magnet: resonant quantum tunnelling in an $S = 12$ molecule, *Chem. Commun.* 2666–2667 (2001).

181. H. Andres, R. Basler, A. J. Blake, C. Cadiou, G. Chaboussant, C. M. Grant, H. U. Gudel, M. Murrie, S. Parsons, C. Paulsen, F. Semadini, V. Villar, W. Wernsdorfer and R. E. P. Winpenny, Studies of a nickel-based single-molecule magnet, *Chem. Eur. J.* **8**, 4867–4876 (2002).
182. S. K. Ritter, Single-molecule magnets evolve, *Chem. Eng. News* **82**, 29–32 (2004).